**Journal of Indian
Institute for Engineering,
Management and Science**
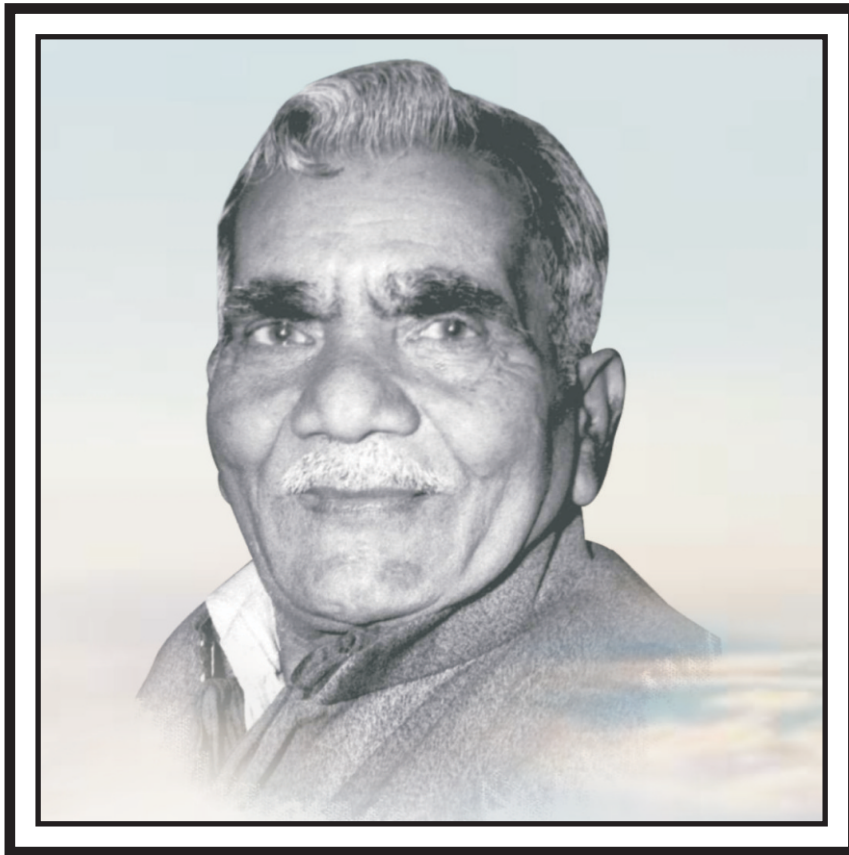
Editor-in-Chief :

Dr. Saket Agarwal

Inspiring Soul

The actual fact of life is,
"To achieve Golden path to success;
one must strive hard from dawn to dusk."
The crux behind this is,
"The hard work that you put in,
will be recognized as an appreciatioin by honor of success."

- Mukut Behari Lal

Editors - in - Chief Message

Dear All,

It's our immense pleasure to introduce you the Volume-2 Issue-I of Journal of Indian Institute for Engineering, Management and Science (JIIEMS). We would like to extend a very warm welcome to all the readers of JIEMS. In this issue, focus is given to publish original research work that contributes significantly to strengthen the scientific knowledge in area of Engineering, Management, Science & Technology. The key focus would however be the emerging sectors and research which discusses application and usability in societal or consumer context whether individual or industrial. Through this journal, we provide a platform for academicians, research scholars and professionals throughout the world to present latest advancements in different areas. Our goal is to take the journal in a direction where it reflects the multidisciplinary nature and becomes the premier journal that covers all aspects of engineering, management, science & Technology.

The success of any journal is built primarily on four groups of people: the contributors, the reviewers, the associate editors, and the publications staff. For this journal, the contributions have come in not only from the academic community but also from the corporate world. We would like to thank all the contributing authors for providing outstanding research articles on a broad range of topics and we hope that the research featured here sets up many new milestones. We appreciate the efforts put by all the editorial team members, reviewers who have helped us in making this journal a possibility. We have had an overwhelming response from some very eminent editors and researchers globally to support as editorial Team. We look forward to make this endeavor very meaningful. We also thank all the publishing staff members and express my sincere appreciation for the support they have given to JIIEMS.

JIIEMS is currently accepting manuscripts for upcoming issues based on original qualitative or quantitative research, an innovative conceptual framework, or a substantial literature review that opens new areas of inquiry and investigation. Case studies and works of literary analysis are also welcome. It would be definitely a privilege to publish a high quality research article which satisfactorily passes the editorial and peer review protocol. On behalf of the advisory board, we welcome your comments, views and suggestions. I hope to be able to bring about gradual changes in the near future for a successful indexation in the prestigious databases and more importantly for the improvement of the journal.

Please direct any manuscripts, questions or comments to: jiiemsr@gmail.com

Editors-in-chief
JIIEMS

Journal of Indian Institute for Engineering, Management and Science (JIIEMS)

Editorial Board

Journal of Indian Institute for Engineering, Management and Science (JIIEMS)

Solar Powered Mobile Operated Grass Cutting Machine

Ritesh Maurya[a], Aditya Srivastava[a], Himanshu Tiwari[a]*, Sarvesh Pal[a], Harsh Singh[a], Subodh Kumar[a], Shashank Dubey[a], Ankush Gaurav[a]

Department of Mechanical Engineering, Uma Nath Singh Institute of Engineering & Technology, V.B.S. Purvanchal University Jaunpur, Uttar Pradesh, India. 222003

*Email: himanshu.vbspu@gmail.com

ABSTRACT

In the present study, the history and gradual advancement of grass cutting machines are discussed. In the direction of technological development, a grass cutting machine is made that works without any type of pollution or loss of energy. This machine contains grass cutter blades and a well-organized wiring system connected with different power motors for controlling the wheels of the automated grass cutting machine. It also contains a 20 watt solar collector and a 12 volt cell. This machine contains smart functions that allow it to cover a whole area of a garden with a mobile device that has a certain range limit for the Bluetooth module. Arduino Uno circuit and Bluetooth module act like the brain of the entire system, which makes efficient directional control on wheels of grass cutting machine. Related calculations are also done to ensure its practical capability.

Keywords: *solar panel, arduino uno, mobile controlled, hc-05 bluetooth module.*

1. INTRODUCTION

In the very beginning, Edwin Budding made a grass cutting machine in 1830 in Thrupp, England [1]. It was designed to cut grass on sports fields and gardens and was granted a British patent in 1830 [2]. This grass cutting machine was pushed from behind. It was soon discovered that there had to be an additional handle in the front to make it easier to tow the machine. These machines were strikingly similar to modern grass cutting machine [3]. His machine was the inspiration for making advanced grass cutting machine for pitches, grass courts, etc. In 1840, some grass cutting machine were made that could be pulled with the help of animals. Amariah got the first USA patent for a spindle grass cutting machine in 1868 [4]. In 1870, Elwood McGuire designed a human push grass cutting machine that was very light and a commercial success. J. Burr got a patent for an improved rotary blade grass cutting machine in 1899 with repositioned wheels for better performance.

In 1893, a steam grass cutting machine was built. In 1900, a very famous grass cutting machine was Ransomes' Automaton, which was available in chain or gear models. Grass cutting machines with gasoline (petrol) engines were developed at the beginning of the twentieth century. In 1902, the first was produced by Ransomes [5]. After World War-I, JP Engineering of Leicester produced very popular chain grass cutting machine, in which operators could ride over the animals that were pulling the big machines. It was the first riding grass cutting machine. 'Ideal Power Mower' made the world's first self-propelled garden tractor in 1922, called "Triplex" [6]. The roller grass cutting machine has changed very little since the 1930s. Gas powered grass cutting machines are used in 90% of US households and generate 5% of total pollution. Today, the world is facing a major pollution problem. Gas emissions from grass cutting machines also create pollution. These are also not economical due to the increased cost of oil. On the other hand, electrically powered grass cutting machines consume a large amount of energy for their operation [7]. Various designs have been developed as per need and convenience, but the overall performance is still not up to level. To overcome these limitations, a solar-powered mobile lawn mower is proposed in this study. Using infinite solar energy, the cell is charged, and then this current is fed to the electric motor, which in turn rotates the cutting blades. This grass cutting machine leads to the improvement of the cordless electric grass cutting machine. In the present study, a remote-controlled grass cutting machine was designed. It is more suitable on hot summer days, when one does not prefer to stay in the sun. The mobile application will allow the user to control the speed and direction of the grass cutting machine. The functional prototype of the smart solar lawn mower focuses on renewable energy sources because primary energy sources have been successfully produced with high working efficiency [8]. The grass cutting machine is suitable for small applications and small grasses due to its short operating time [9].

2. COMPONENTS AND MATERIALS

25-mm-diameter PVC plumber's threaded pipes, T-sockets, elbows, etc. were used to create the basic structure. The purpose behind making a frame of PVC material is to provide light weight and good impact resistance. Stainless steel was chosen as the material for the sharp blades of the grass cutting machine. Stainless steel was selected as it has good corrosive resistance because, during grass cutting, moisture or water in grass has a tendency to generate corrosion on blades. A 12 V, 3 Ah cell is used to store energy. Two types of motors, such as a high-speed motor (2400 rpm) for cutting knives and a metal gear motor (which has a lower speed but more power), are connected to the rotating wheels. 4 rubber wheels with a diameter of 100 mm and a 20 W solar panel were taken.

The microcontroller board used in the design is an Arduino Uno L293d motor driver used to drive a metal gear motor for smooth and quiet operation. This driver board receives the control signal from the microcontroller board. Bluetooth module HC-05, intended for transparent setting of wireless serial connection. Connecting wires were used to connect the copper wires and to connect the circuit. In addition to these switches, they were used to control the mechanism, charge indicator, etc.

3. DESIGN AND FABRICATION

First, PVC pipes were cut to the required lengths and joined with elbows and T-sockets to form a rectangular structure. Then the engine with the blade is connected, and this arrangement is connected to the frame with a socket. The blade is mounted on the underside of the grass cutting

machine on the motor shaft. Four wheels are then attached to the frame. The wooden layer is connected to the PVC pipe at the desired place to insert the battery. Then the 12V electric DC motor is placed and fixed with supports in the center of the wooden layer. Then Arduino board was connected to the L293d motor driver by putting it in parallel. Then the BT module HC-05 was connected to the motor driver with a jumper wire. An emergency electrical power port and charging indicators were then attached.

Table.1. Technical Specifications

Motor torque (60 rpm)	15 kg-cm
Blade motor	2400 rpm
Cell Specification	12V/3Ah
Cell full charge duration	2 to 3 hours
Shearing height	1.5 cm
Wheel radius	50 mm

Figure.1. Assembly of grass cutting machine
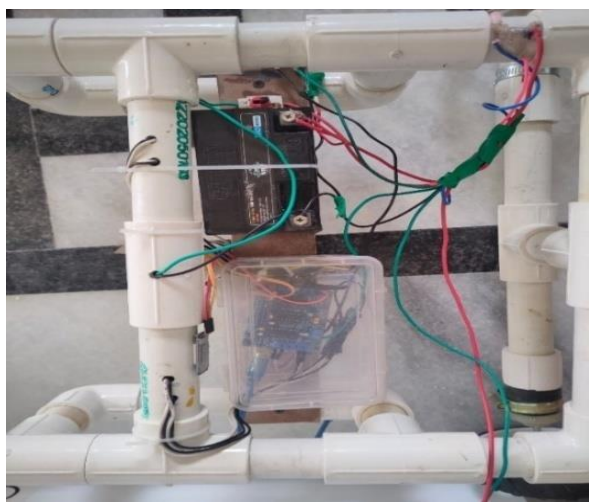
Figure.2. Wiring and connections

4. CALCULATION PART

Torque of wheel motor

Cell capacity: 12 V, 3Ah

Power Produced: $12 \times 3 = 36$ Wh
Engine speed: 60 rpm

Hence total torque of motor $T = \dfrac{60P}{2\pi N}$

Where P is in watt and N in rpm

$T = \dfrac{60 \times 36}{2\pi \times 60}$

$T = 5.732$ N.m

Hence torque per wheel $= 5.732/4 = 1.433$ N.m

Torque of Cutter Blades

Cell capacity: 12V, 3Ah
Cell power: 36 Wh
Motor speed: 2400 rpm

Hence total torque of cutter blade $T = \dfrac{60P}{2\pi N}$

Where P is in watt and N in rpm

$T = \dfrac{60 \times 36}{2\pi \times 2400}$

$T = 0.1433$ N.m

Load Produced by Cutter Blades

As Load $= \dfrac{\text{Torque (in N.m)}}{\text{Radius (in m)}}$

Load $= \dfrac{0.1433}{0.01}$

Load $= 14.33$ N

Charging Time of Cell

Capacity of solar collector: 20 w, 12 v

Current (in A) $= \dfrac{\text{Power (in W)}}{\text{Voltage (in V)}}$

Current $= \dfrac{20}{12}$

Current $= 1.6667$ A

Charging time $= 12$ Ah$/1.6667 = 7.2$ hours

$= 7$ hours 12 minutes

5. WORKING PRINCIPLE

When it comes to the operation of the smart grass cutting machine, the panels are placed on top to quickly receive high-intensity sunlight. As sun is the main and unlimited source of energy for life on Earth [10]. Solar collectors convert the energy of the sun into electricity. Cells are now used to store this electrical energy. The motor is connected to these cells using connecting wires. A total of five motors were used here, out of which four were used to drive the wheels of the grass cutting machin and one motor was used to drive the cutting knives. The blade thus rotates at high speed and cuts the grass. The motors are connected to an Arduino Uno, which regulates their direction of movement. The relay that is connected to the

Figure.3. Circuit Diagram of arduino uno

Arduino Uno is connected to one of the grass-cutting motors. The Arduino Uno has been pre-programmed to send signals via a Bluetooth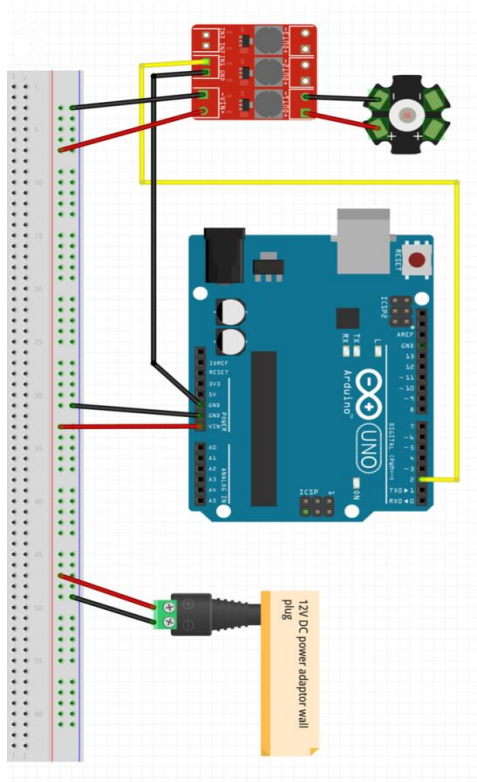 transceiver, allowing it to be easily detected by mobile phones. The connection pins connect the Arduino, motor controller, and relay to the Bluetooth transceiver, allowing data to be sent to the configured device. The Bluetooth transceiver transmits the incoming signals and completes the setup by sending the waves to the designated device and cutting the grass. Connection pins, often known as jumpers, are used to transfer data from one component to another. Using the application software loaded on the phone, the functions of the phone can be controlled from a specific range.

6. CONCLUSION

The purpose of this project is to design and build a smart grass cutting machine that uses an Arduino Uno instead of a Raspberry Pi to produce higher I/O. A PVC frame is used to create the structure due to its light weight and anti-corrosion properties. The wiring is also done through inside of these tubes to protect the wires. The entire setup is remote controlled. Various related calculations were also done to find out the actual capability of the machine. To the best of our knowledge, the above combinations have not been previously reported. As the technology goes through the process of upgrading every day, the smart solar lawn mower can be further developed by the industry.

REFERENCES

[1] Ms. Rutuja, A. Yadav, Nayana V. Chavan, Monika B. Patil, V.A. Mane., 2017., "Automated solar grass cutter", International journal of scientific development and research (ijsdr), vol.2.

[2] Everett G., 1869, "Improvement in Lawn-Grass cutting machine", pg 1

[3] Mower History, 2011, "The old grass cutting machine club",

[4] Mary B., 2010, greener pasture, history of lawn mover

[5] Ransomes automation, grass cutting machine club, 2023 Ideal power lawn mower, reoldsmusem.org

[6] Dipin.A, Dr. Chandrasekhar. K. 2014. Solar powered vision based robotic lawn mower, international journal of engineering research and reviews, vol. 2, p 53-56.

[7] Jain V., Patil S., Bagane P., Patil S., 2016. Grass cutter, international journal of science technology and engineering, vol. 2, p 576-580.

[8] Prabha S., Biradar D., Panshette S., Veernhadrappa. 2016. Solar grass cutter machine, international journal for technological research in engineering, vol.3, p 2702-2706.

[9] Patil B., Patil S., 2017. Solar based grass cutting.

Numerical simulation of shock wave diffraction over curved walls

Sanhin Kumar Singh[a*], Abhishek Kundu[a], Sanjeev Kumar Arya[a]

[a]Department of Applied Mechanics, Motilal Nehru National Institute of Technology Prayagraj- Allahabad, 211004,India

*Email: sachinsingh2255@gmail.com

ABSTRACT

When a regular travelling wave passes through a sudden area expansion, shock wave diffraction develops. The flow properties are described by the words turbulent, compressible, and vertical, which are gradually smeared out due to turbulence's dissipative nature. The investigation of these phenomena reveals numerous flow patterns, including shear layer generation, vortex development, and vortex/shock interaction. Shock wave motion is significant in many disciplines of engineering, and it is becoming increasingly important in medical applications and inertial confinement fusion techniques. Moving shock waves form complicated flow structures when they encounter a change in area, which can be difficult to comprehend. Experiments and other numerical analyses have been conducted by previous scholars to investigate this issue in greater depth. There was a gap between numerical and experimental work that had gone unsolved. One of the goals of this research is to study the disparity between numerical and experimental work, as well as what experimental approaches are appropriate for this type of work and how they should be implemented. The majority of past research has focused on abrupt changes in geometry that result in immediate flow separation. In characterising high-speed flow around complex structures, accurate prediction of the impacts of a neighbouring wall on the global flow behaviour behind a diffracting shock wave is critical. Using numerical analysis, this study investigated the near-wall impacts on flow patterns behind a diffracting shock wave on curved walls. Curved walls will also be examined in this study, as well as complex flow features. To explore the effect of shock waves on the flow field produced and to compare with previous work, numerical simulations were performed using the ANSYS Fluent to explore the impact of a shock wave on the flow field created and to compare it to a different turbulence model, such as the K-omega, k-epsilon, and SST transition models.

Keywords: shock wave, diffracted shock wave, curved wall

1. INTRODUCTION

High speed non-stationary flows are characterized by shock waves which affect the efficiency and control of aircraft, and supersonic flow devices. The high acceleration of current flying vehicles, the selection of optimal projectile/missile designs, and research on the flow behavior behind a shock wave diffracting over complex convex barriers is motivated by advancements in engine intake and exhaust systems. The effect of the near wall on the global flow field must be explored in order to understand the complicated flow structure behind a diffracting shock wave. To make accurate forecasts of flow features at the wall surface, the behavior must be understood. Skews' previous work ([1], [2]) concentrated on basic convex walls, with a particular emphasis on the diffracting shock wave's shape while a later investigation by Skews [3] on circular arc and multifaceted walls did not comprehensively discuss the near wall effects on the flow pattern. Law et al. [4] investigated the near wall effect on curved and multifaceted walls but the transient development of the flow features were not exhaustively explained. The current study examines the impact of a near wall on the flow field behind a shock wave diffracting over a curved wall and Numerical simulation of different turbulence model such as k-omega, k-epsilon and SST transition model.

Normal shock waves can additionally be seen as fixed waves comparative with a wing on a flying plane for example, or as precarious moving waves comparative with a proper lab perspective. An unstable shock wave is generally characterized as a non-straight wave which goes at supersonic rates. It is pictured as a acute minor wave front across which a portion of the stream properties, for example, pressure, temperature, thickness, entropy and speed of stream change unexpectedly. The thickness of a shock wave is tiny contrasted with different lengths qualities of liquid stream. Temperamental shock waves can happen normally as on account of a seismic tremor, volcanic emission also lightning bolt. A portion of the man caused guides to remember explosion for mining or development. They are usually created unexpectedly which lead to unwanted 5 outcomes, for example extraordinary clamor levels, pressure loads, sonic blast, and so forth Shock waves produced by blasts cause harm and may bring about fatalities. Shocks should be weakened rapidly in mines and passages to guarantee wellbeing. Pressure weakening of a moving amazement engendering in a pipe is fundamental in heaps of uses, like wellness and wellbeing, transportation (extreme speed trains and vehicle silencers), and the synthetic business (pipe stacking). At the point when considered o openings, vessels, aggregators, shut cylinders, move portion decreases, or valves, those strain waves as often as possible explanation unreasonable stacking on funnelling structures in business and thermal power stations, and while contemplated o holes, vessels, gatherers, shut cylinders, move fragment decreases, or valves, they can reason large strain increment (Movahed and Groenig, 1986).After a duration of time, the strain waves merge, turning into more potent and, in a few cases, forming new surprise waves. Due to their abrupt front, those surprise waves create better stresses in brief tubes than strain waves of similar power however longer extensions. In exhaust ducts and tunnels, strain attenuation of those surprise waves is inherently present, with the roughness of the partitions gambling a key component within side the strain attenuation upstream. Previous research (Igra et al., 2001) has revealed. When a surprise wave propagates right into a branched duct or into massive damping chambers, the foremost mechanism answerable for lowering the surprise wave is more than one enlargement waves created through grooves and branched junctions. Amplification of surprise waves, on the opposite hand, has been stated because of more than one reflections or compression waves. The improvement of numerical techniques to interrupt the conservation legal guidelines for

compressible overflows, particularly the Euler equations, has matured. In the beyond few decades, a number of numerical schemes with high-order delicacy had been developed (Toro, 1999). The majority of them produce super consequences on each based and unstructured morass, and had been prolonged to extra complicated bodily systems. Due to the quick take a look at time, surprise tube flows are characterized through shakiness. The computational findings of the risky Euler equations had been used to correctly constitute surprise propagation, reflections from walls, and frame commerce. For example, the disparity among experimental prints and numerical findings of the Euler equations in surprise surge fastening in a massive chamber may be significant.

Shock diffraction, among the most important discoveries in surprise factors, has been proven numerous times as a numerical test for the computerization of unsteady compressible overflows. During the 18th International Symposium on Shock Swells, traditional check of surprise diffraction round a 90-diploma nook becomes organized; Takayama and Inoue highlighted diverse numerical and experimental consequences (1991). By evaluating numerical consequences of the Euler equations with experimental prints, it's far clean that high-order Godunov-kind schemes, piecewise parabolic system (PPM), finite quantity Galerkin scheme (FVGS), FEM-FCT, TVD-kind schemes, or different schemes can correctly reproduce diffracting surprise swells, growth swells, and the form of the principle whirlpool.

2. METHODOLOGY

The analysis was done using numerical techniques. The Numerical method chosen, involved solving the Reynolds Averaged Navier-Stokes (RANS) equations with K-omega, K-epsilon and Shear Stress Transport (SST) turbulence model. The characteristic length was obtained by utilising the radius of the curved wall as the flow domain. The inlet and outlet boundaries are as shown in below figure, with the primary flow direction from left to right. All other boundaries were no-slip walls.
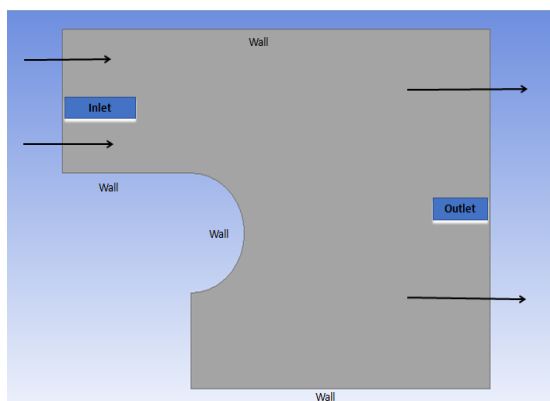

Figure.1. The flow domain for the simulation

The inlet boundary is two trademark lengths high and three trademark lengths upstream of the beginning of the divider shape, to take into account the damping out of mathematical commotion emerging from the imprudent beginning of the stream at the channel. The outlet is three typical lengths downstream of the curved wall and four characteristic lengths tall so that the flow along the wall is not affected by the

outflow boundary. The flow domain was discretised using structured mesh. The numerical analysis was carried out on an Intel i7, 3.40 GHz CPU with 6 GB of RAM and each simulation took about 6-8 hours.

2.1. Geometry and meshing

The domain of the flow is defined using a curved wall which is having some radius as feature length. The entry limit was feature length four and feature eight the height of the river at the beginning of the bending of the wall. Exit point the boundary was 16 elements long and 12 cubits long feature height below curved wall. These the length is chosen so that there is a sufficient space from inlet for any sound produced by impulsive the start of the flow will decrease again. It will not interfere with the flow if you order the shocking interaction of the incident with the exit border to the area of interest the duration of the estimated test periods. At hundred mm feature length, it means the proportions of the entry and exit limits are the same as the size of shock tube. All borders were not the entrance or exit the boundary was set as fixed temperature, fluid limits. The background was started in typical atmospheric conditions; then the inlet was placed at a fixed speed inlet at a temperature, pressure and speed similar to that of flow after a ordinary shock to the estimated Mach number calculator. Exit border separated from the flow after the shock and for a long time as an exit point the border is far sufficient; the border can be hard wall and should not strongly affect the results. In this a case of twelve length features seems to suffice.

(a)   (b)

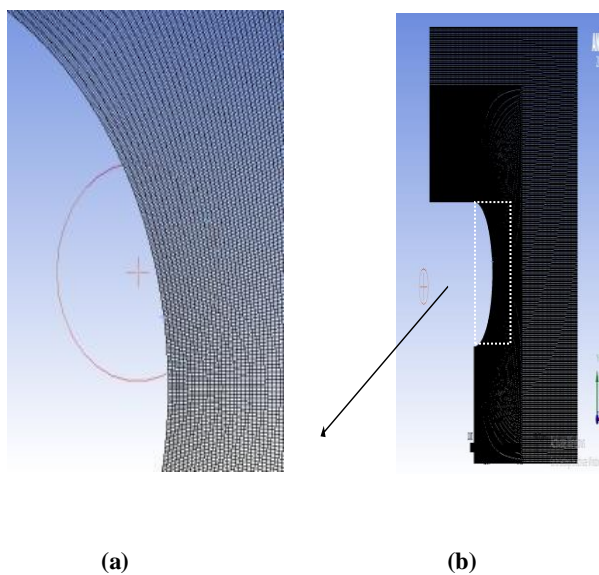**Figure.2. (a) Zoomed view of Structure Mesh, (b) Structure Mesh**

3. RESULTS AND DISCUSSION

The flow domain behind the diffracting shock is divided into three regions after the start of separation: steady expanding gas upstream, complex flow region and the compressed flow downstream. These regions were developed as a result of the diffraction of the incoming shock wave as it moved on the curved wall.
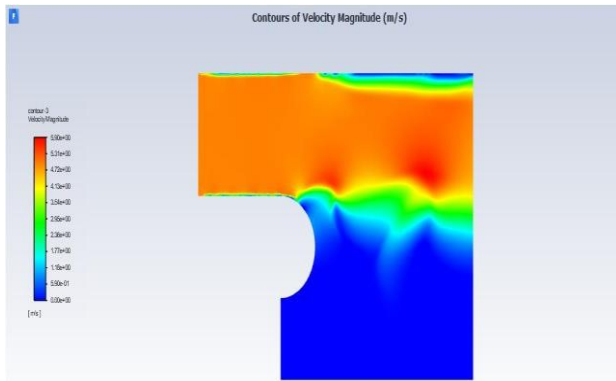
3.1 Pressure Contour and Velocity Contour

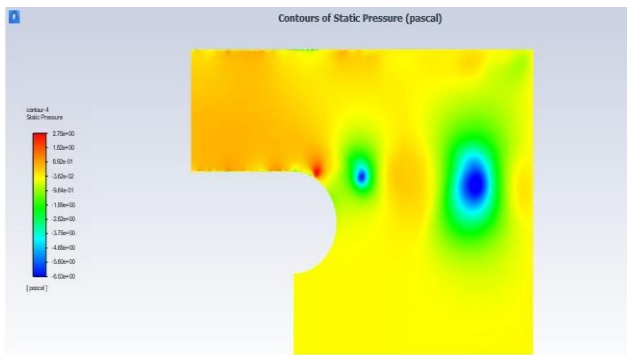**Figure.3. (a) Pressure Contour**

Figure.3. (b) Velocity contour

3.2. Boundary conditions and solver setting

The numerical analysis is carried out with the sales Navier-Stokes (RANS) Central Reynolds Solution Code, particularly the ANSYS Fluent. The law of ideal gas The model was solved using a hybrid solver that took into account both congestion and Menter's [13] By C. Law et al., Shear Stress Transport (SST) k-order Model. Because it combines k- and k-turbulence models to employ a nearby wall k-model durability and k-turbulence model streaming free accuracy, the SST turbulence model was chosen. This is significant in light of the fact that the field of flow has areas of strong vorticity that are spaced apart by up to and flow separation. The mineral-based approach employs an algebraic multi grid method along with a Gauss-Seidel-based line equation solution [14]. A primary cell code called ANSYS Fluent Release 2020R1 employs a variety of different approaches to assess the flexibility of cell boundaries. A clear schedule based on current data, such as advanced choices, is worth the investment when a system with second order increase is chosen for the one-time split. Courant number is set to 1.5. Gradient's number limits there are those that ensure stability in the separation of air schemes; deficit setting uses least modulus the task of cutting off many shoots and less when rebuilding numbers on the surface of the cell [14]. Default limit saved as a first order solution for all types of discontinuation.

Table .1. Parameters

Parameters	values
Gas (air) velocity (m/s)	514.5
Turbulent kinetic energy	0.09375
Specific Dissipation Rate(1/s)	641.8003
Density of air (kg/m$^{2)}$	1.225
Temperature(k)	288.16
Viscosity of air (kg/m-s)	1.7894e-5
Ratio of specific heat	1.4

3.3. Validation of turbulence model of different radius of curved wall

(a) Radius=25mm
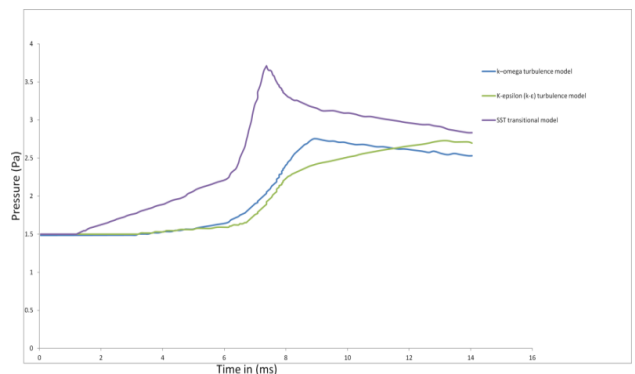
Figure.4.(a) Validation of turbulence model(R=25mm)

(b) Radius= 100 mm
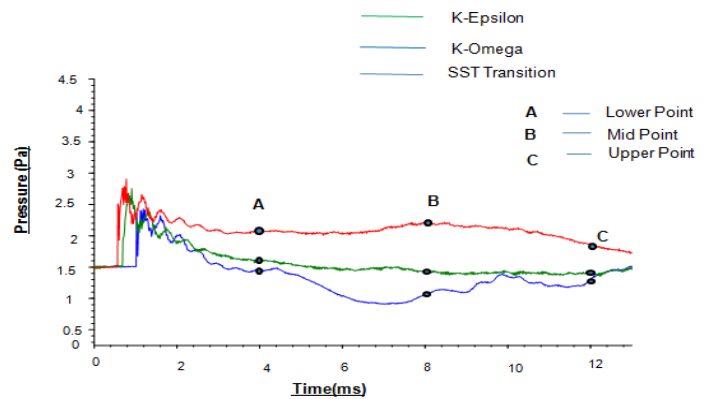
Figure.5.(b) Validation of turbulence model(R=100mm)

3.4 Percentage Error

Table.2. Error in wall pressure

SR.N.	Time(ms.)	Wall Press. (self)	Wall Press.\ (References)	% Error
1.	2	87000	87000	0
2.	4	140000	129500	7.5%
3.	6	186000	164610	11.5%
4.	8	210000	184170	12.3%
5.	10	256000	216576	15.4%
Net Percentage Error				

3.5 Grid Independent Test
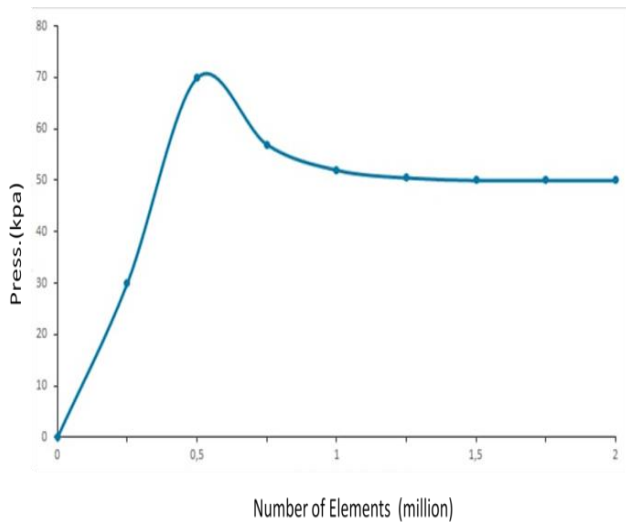
Figure.6. Gride independent test (c)

4. CONCLUSION

Understanding the complicated go with the drift shape at the back of a diffracting surprise wave calls for that the impact of the close to wall on the worldwide go with the drift subject be studied. The behaviour ought to be understood that allows you to make correct predictions of the go with the drift capabilities on the wall surface. As the inlet velocity increases, the shock wave diffraction on the curved surface increases.

The conclusions of this study are divided into Four main sections:

- Investigation of different Turbulence models.
- Investigation of the Curved wall surface.
- Quantitative Validation of three turbulence model (K-omega, k- epsilon SST model.
- In Grid Independent Test maximum pressure obtained at 0.5 million elements.

The numerical simulations proved significantly more challenging for the round geometry due to the presence of viscous phenomena in the flow.

REFERENCE

[1] Skews BW. The shape of diffracting shock wave. Journal of Fluid Mechanics;1967, Vol. 29, p. 297 –304 Doi:10.1017/s0022112067000825
[2] Skews BW. The perturbed region behind a diffracting shock wave. Journal of Fluid Mechanics; 1967,Vol.29,p.705.Doi: 10.1017/s0022112067001132
[3] Skews BW. Shock wave diffraction on multi-faceted and curved walls, Shock Waves; 2005,14,3,p.137 – 146.Doi:10.1007/s00193-005-0266-5
[4] Law C, Skews BW, Ching K.H. Shock wave diffraction over complex convex walls. 26th International Symposium on Shock Waves, Göttingen; 2007. Doi:10.1007/978-3-540-85181-3_109
[5] Sun M, Takayama K. A note on numerical simulation of vortical structures in shock diffraction. Shock Waves 2003,13: p. 25 – 32. Doi: 10.1007/s00193-003-0195-0
[6] Sun M, Takayama K. The formation of a secondary shock wave behind a shock wave diffraction at a convex corner, Shock Waves 7; 1997, p. 287 – 295. Doi:10.1007/s001930050083
[7] Menter FR. Zonal two equation K-w Turbulence;2012. Doi:10.2514/6.1993-2906
[8] Law C, Menon N, Skews BW: Near-wall features in transient compressible flow on convex walls, ISSW 25, Bangalore, India, 2005. Doi:10.1007/978-3-540-85181-3
[9] Law C, Felthun LT, Skews BW: Two-Dimensional Numerical Simulation of Shock-on-Shock Interactions, ISSW 23, Fort Worth, Texas, 2001
[10] Takayama K, Inoue O: Shock Waves 1, 4 (1991) 301 – 312. Doi:10.1007/BF01418886
Whitham, G.B.: J. Fluid Mech. **2**, 145–171 (1957).Doi:10.1017/S002211205700004X [12]
[11] Sun M, Takayama, K.: Shock Waves **13**, 25–32 (2003).Doi:10.1007/s00193-003-0195-0
[12] Law C, Muritala AO, Skews BW.Unsteady flow with separation behind a shock wave diffracting over curved walls. Shock waves;2013 Springer-Verlag Berlin Heidelberg ,2013. Doi:10.1007/s00193-013-0486-z
[13] ANSYS® Fluent, Release 2020R1, Help System, Theory Guide, ANSYS Inc.

Effect of Explosion Load Induced by the Placement of an object at the exit of a Shock Tube: a Computational Study

Nihal Pandey[a*], Abhishek Kundu[a] , Prerak kumar Swami[b]

[a] Department of Applied Mechanics, Motilal Nehru National Institute of Technology
Allahabad, Prayagraj, 211004, India
[b] Department of Civil Engg., Rajshree Institute of Management & Technology,
Bareilly, 243123, India
*E-mail: pandeynihal55@gmail.com

ABSTRACT

Blast waves are studied numerically either by taking the fluid flow as inviscid or using a turbulence model. This research looked at how introducing a larger or smaller object into the open end of a shock tube could affect the blast wave's impact on a wall downstream. An object is inserted inside a shock tube. Blast wave is generated using a shock tube. ANSYS Fluent is utilised for simulation, and structured mesh is employed. Initial pressure in the driven part is atmospheric, whereas initial pressure in the driver section has a pressure ratio of 40. Computational Fluid Dynamics simulations were performed to research the impact wave generated by a impact wave and the explosion load caused by the pressure distribution on an object inside a shock tube at a certain distance. [1] Today, commercial and military buildings and vehicles need explosion wave mitigation more than before. An object is inserted inside a shock tube for the reduction of blast load on an exit of a tube. Blast waves interacting with different size objects are placed at the same locations in this study for a pressure ratio of 40. By numerically solving the unsteady, we can simulate the detonation of a blast generated in a shock tube. After all the observations, our final conclusions are that the pressure force varies with the size of the object in the shock tube and the positions of the object, the higher the size of object, the greater the pressure force generated. if it's in close proximity to the shock tube., so the faster and more pressure, the force will be generated. This study will be extremely useful to understand the effect of blast waves and very helpful in mitigation of blast waves.

Keywords: shock tube, blast wave, k-epsilon model, driver section, driven section

1. INTRODUCTTION

When initially high pressure is created on driver section and atmospheric pressure is created on driven section after that flow moving from high pressure to low pressure and after that blast waves are reflected by walls and other surfaces in shock tube, they become more influential, creating greater damage than high explosions in similar spaces. A scan of major terrorist acts over the previous few decades reveals a dramatic increase in the number of people killed or injured by blasts, as well as significant economic damages. Scientists and engineers have become more aware of the breakdown of engineering buildings and materials under blast loading as a result of repeated terrorist attacks. Blast wave analysis is required to anticipate the behavior of buildings under blast loads. When initially high pressure is created on driver section and flows moving from high pressure to low pressure and at the end of

driver section due to atmospheric pressure is created on driven section after those high pressure which rupture the diaphragm section and After the diaphragm, the high pressure is transformed into a high pressure wave, which then generates the blast wave.

In this study, we examined the efficacy of dispersing numerous objects of differing sizes and locations along the wall downstream of the exit of an open-ended shock tube. and determined the amount of force exerted on each object. The analysis was done by using computational methodology for calculating the pressure distribution on wall by performing CFD simulations. In this investigation, the pressure distribution on the wall was determine is compared for five distinct scenarios: no object, an item put at a distance of 5D, an object put at a separation of 6D, an object positioned at a distance of 7D, and an object positioned at a distance of 8D; a multi-object scenario is also investigated. Both a 40:1 and a 50:1 pressure ratio are modeled and simulated.
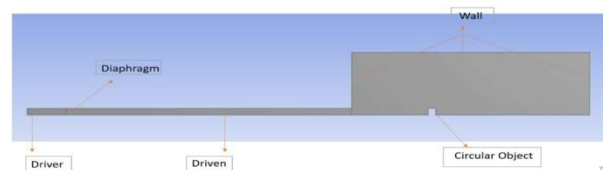
Figure.1. Computational Domain

Kleine et al. (2005) generated the blast waves using explosive charges to carry out the experiments related to blast waves. Sadot et al. (2017) generated the blast waves using explosive wires to carry out the blast wave experiments. They presented a method to produce laboratory-scale, controlled explosions. Using various types of chemicals blast waves are generated for experiments (Borisova et al, 2009; Ishii et al. 2018). Arakeri et al. (2004) studied the generation of the vortex ring along with the shock wave diffraction from the shock tube open end using the particle image velocimetry.

Experimentally investigating the explosion is costly. A limited number of results are also extracted from an experiment. Consequently, numerical simulations are performed. Kumar et al. (2020) exhaustively analysed the diaphragm rupture pressure, length of driven section, and gas inside the driver section of a shock tube. They examined how pressure affected the shock tube at different locations. The effects of shock tube geometry on the propagation of the ideal detonation wave profile were evaluated by Li et al. (2017). Researchers solved multi-component Navier-Stokes equations to analyse flow dynamics at 13 and 57 diaphragm pressure ratios. The mirrored blast wave combined with the shock wave at PR 13.

Dispersed and reflected wave interaction gives the trailing jet multiple triple spots and a PR value of 57. Blast wave genesis and jet interaction with objects generate more vorticity than blast wave diffraction and primary vortex ring formation, according to the enstrophy graphic.

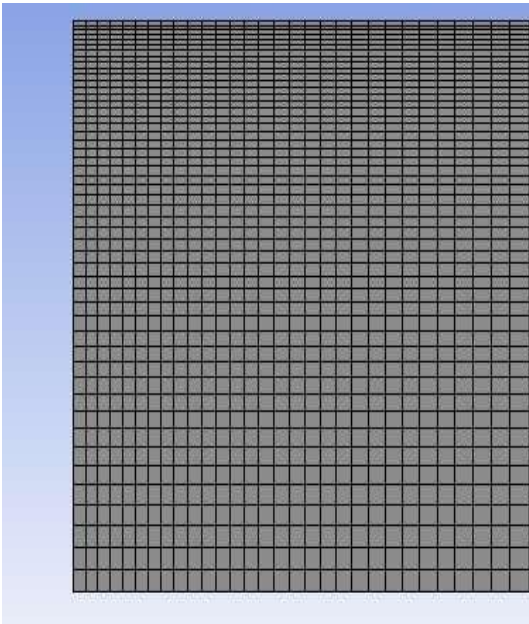By putting something between the tube's exit and the wall, the blast can be made less powerful. For this study of how explosion waves interact with round objects, four places were chosen with pressure ratios between 40 and 50. By using the AUSM scheme and the 3rd It is possible to simulate blast detonation in shock tubes using the Order Monotone Upstream Centred Scheme for Conservation Laws (MUSCL) scheme for solving unstable, axi-symmetric N-S equations.
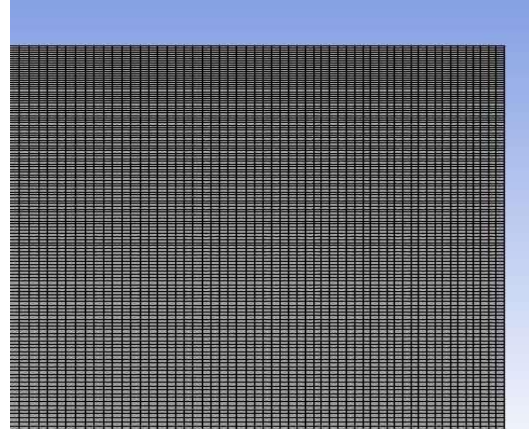
The force of a blast on a wall goes down if an object is close to where the shock tube comes out and up if the object is moved closer to the wall. After that distance, it is nearly constant. The CFD results demonstrate that shock tube pressure ratio increases wall peak pressure. The K-ε model is intended for aerospace applications and effectively addresses boundary layer issues. 2013 (ANSYS Fluent Guide).

2. METHODOLOGY

ANSYS software tools are used for the simulation work. Computational domain is two-dimensional. Geometry is designed using the Design Modular. The driver's section is 165mm long and the driven segment is 1200mm long. Diameter of the shock tube is 64mm. The shock tube exit is into the rectangular box of size 1000mm × 600mm. As the shock tube's shape is uniform about the axis that is horizontal, only half of it is simulated to reduce computational time. Meshing is done using the meshing tool available in the ANSYS workbench. Minimum orthogonal quality of the mesh is 0.999988, maximum orthogonal skew is 1.72853e-06 and maximum aspect ratio is 19.63. There are a total of 175,000 parts, and there are a total of 176451 nodes. Solver is density based. Pressure in the driver section is 4000000 Pa. and 101325 Pa. in the driven section. All boundaries except the axis are taken as wall.

(a)

(b)

Figure 2. Grid zoomed at (a) front side of the driver section (b) Backside wall

2.1 Governing equation

The Navier-Stokes equations regulate CFD. It relies on the physical properties of the fluid conservation law. For explosion wave simulations, the continuity equation, energy conservation equation, equation of state, momentum conservation equation and turbulence modelling equations are the equations for 2-dimensional, unsteady, compressible flows. These equations are expressed in differential form as

2.1.1 Continuity equation

$$\frac{\partial p}{\partial t} + \frac{\partial p U_i}{\partial x_i} = 0$$

$$\rho \frac{\partial U_j}{\partial t} + \rho U_i \frac{\partial U_j}{\partial x_i} = -\frac{\partial p}{\partial x_j} - \frac{\partial \tau_{ij}}{\partial x_i} - \rho \vartheta' u'$$

2.1.2 Momentum equations

$$\underbrace{\rho \frac{\partial U_j}{\partial t}}_{1} + \underbrace{\rho U_i \frac{\partial U_j}{\partial x_i}}_{2} = -\underbrace{\frac{\partial p}{\partial x_j}}_{3} - \underbrace{\frac{\partial \tau_{ij}}{\partial x_i}}_{4} - \underbrace{\rho \vartheta' u'}_{5}$$

Where

$$\tau_{ij} = -\mu \left(\frac{\partial U_j}{\partial x_i} + \frac{\partial U_i}{\partial x_j} \right) + \frac{2}{3} \delta_{ij} \mu \frac{\partial U_k}{\partial x_k}$$

1: Time dependent local exchange

2: Convection due to momentum

3: Pressure force

4: Reynolds stress due to turbulence

5: Momentum exchange of molecule (diffusion)

2.1.3 Energy equations

$$\underbrace{\rho c_\mu \frac{\partial U_j}{\partial t}}_{1} + \underbrace{\rho c_\mu U_i \frac{\partial T}{\partial x_i}}_{2} = \underbrace{-P \frac{\partial p}{\partial x_j}}_{3} + \underbrace{\frac{\partial^2 T}{\partial x_i^2}}_{4} \underbrace{-\tau_{ij} \frac{\partial U_j}{\partial x_i}}_{5}$$

1: Local energy change with time

2: Convective flux term

3: Work due to pressure

4: Heat flux term (diffusion)5: Mechanical energy is

5: Transferred to heat in an irreversible manner

2.1.4 Equation of state

For a perfect gas

$P = \rho RT$

Where P represents absolute pressure of gas, and ρ represents density, R represents universal gas constant and Trepresents Temperature.

2.2 Boundary conditions and solver setup

Prior to hitting the shock-absorbing tube, the motorised part is subjected to one atmosphere of pressure and three hundred kelvin of temperature. Air is a medium that is utilised all over the world due to the nearly ideal qualities that it possesses. In two different instances, the patches in the driving region are both squeezed and subjected to an intensely high temperature. Shock tubes with diaphragm pressure ratios of 40 and 50 were utilised in order to produce a scenario that was identical to the original. Rankine - Huguniot conditions were used to compute thetemperature and density of the driving section. The pressure distribution on the wall caused by the shock tube's pressure explosion was simulated in this study using commercial ANSYS Fluent software. The table below shows the initial conditions for two of the simulation situations. In figure depicts the problem's boundary conditions.

Table.3. Initial conditions used for the current simulations

Test cases	P_1 (atm)	$\rho 1$ (Kg/m³)	T_1 (K)	P_2 (atm)	ρ_2 (Kg/m³)	T_2 (K)
1	1	1.17	300	40	6.17	2280
2	1	1.17	300	50	6.29	2800

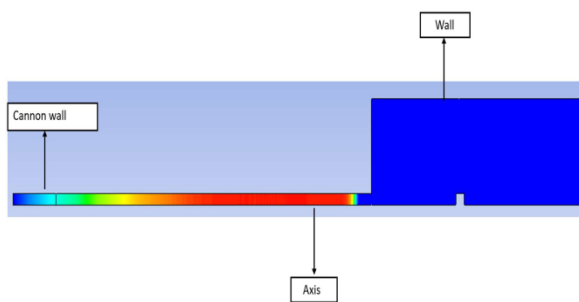## 3. RESULTS AND DISCUSSIONS

Figure.3. Computational domain

The study focuses on shock tube axis and wall pressure distribution. Shock tube diaphragm separates gas in the driver part, at higher pressure, and the driven section, at atmospheric pressure and going from high to low pressure. It ruptures the diaphragm at the driver section's end, sending a supersonically high-pressure blast wave against the wall. The blast wave expands spherically outward at the shock tube exit and is stronger along the shock tube axis. Air pressure exists until the shock tube blasts the wall. Blast waves peak and then drop to

air pressure when reflected by walls. For comparison, shock tube inlet pressure was X=2.36 metre. Peak wall pressure increases with pressure ratio (Figure 3(b)). The time to peak pressure reduces as the pressure ratio increases. Blast wave from simulation hits wall in 4 ms and is 2.36 m from diaphragm to opposing wall. Blast waves travel 542 m/s. All limitations are walls, so the blast wave hits them, reflects back, interacts with other walls' blast waves, and hits them again. This continues until blast wave energy dissipates into the fluid, boosting its temperature. Shock tube axis and wall pressure distribution are studied. The blast wave spreads spherically at the shock tube exit and is stronger along the shock tube axis. Air pressure exists until the shock tube blasts the wall.

In the driver section of the shock tube, initially, Pressure is 40 bar and density is 46.2 kg/m³. After busting of the diaphragm, along with the blast wave, high-density gas in the driver section also moves through the driven section and comes out of the Shock Tube exit.

In figure 4(a), (b), (c), (d) the pressure contour at 3.2ms there can be seen small vortices are formed in the flow domain wherelow pressure region is observed that when simulation is carried out using k-ε model the showing curve is the blast wave. Reflected blast waves from the top and bottom wall can also be seen. In the contour plot only compression wave can be seen,because in the region of the compression wave velocity divergence is negative. Pressure in driver section is very high and afterstriking with the object high turbulence is create and which wave motion is vary with time. In which we observe the wave variation in different size object

(a)   (b)

(c)   (d)

6333   334923

Figure 4. Comparison pressure contour for (a) With no object, (b) With one object, (c) With two objects, (d) With three objects. (Pressure in Pascal)

In figure 5 (a), (b), (c), (d) the velocity divergence contour at 4.1ms in this we can see that when there is no object the blast directlygoes and strikes the wall can see that figure 5 (a) now when we put ne object in front of the blast wave and exit of the shock tube the blast get mitigated and we can that in figure

5 (b) where the velocity curl becomes drastically low after the object but when we two object in front of the blast wave at exit of the shock tube the velocity curl again increases after striking both the object, we can see that in figure 5 (c) now coming to the fourth figure that is figure 5 (d) and comparing with other contour, here blast wave gets mitigated after striking three object but compare to one object it is considerable low.

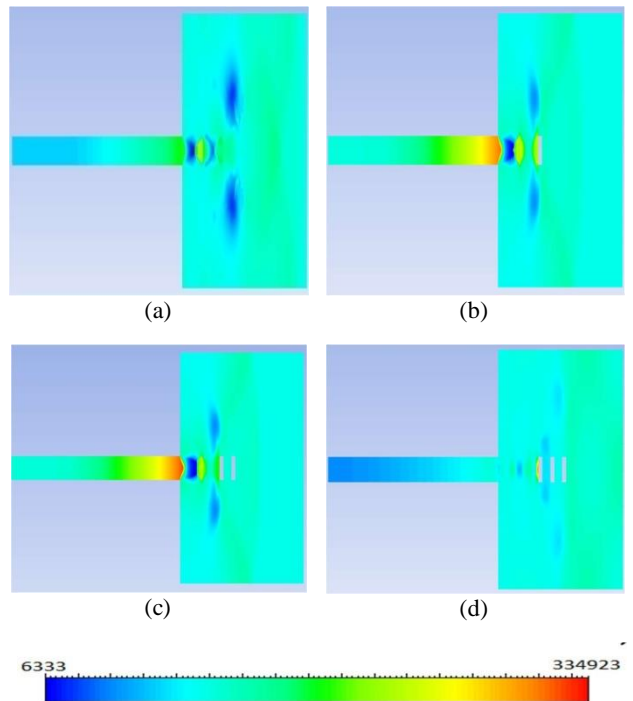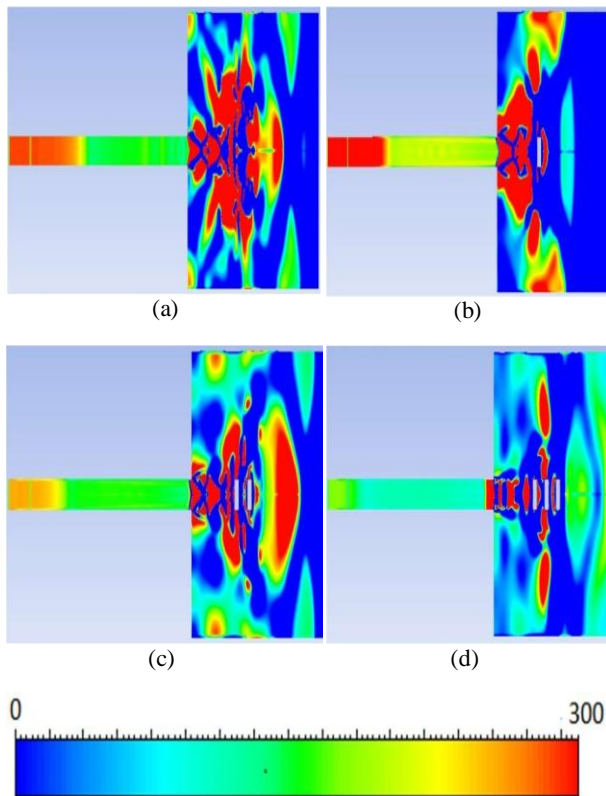(a)   (b)

(c)   (d)

0   300

Figure.5. Comparison Vorticity contour for (a) With no object, (b) With one object, (c) With two objects, (d) Withthree objects.
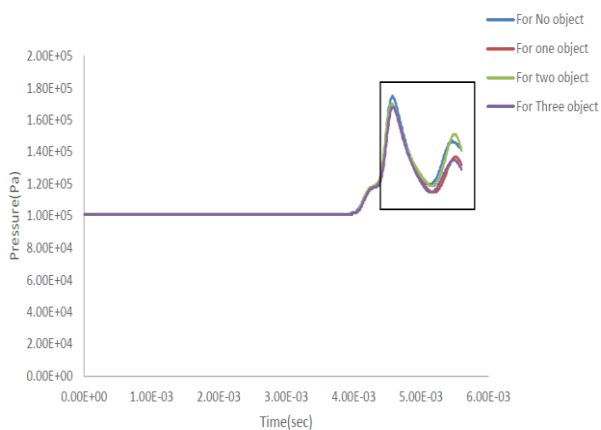
Figure.6.(a) comparison of pressure distribution on wall when placing multi object at exit of shock tube

My final conclusion that by comparing all the contour we can say that blast is well mitigated only there is one object but we increases number of mitigated but comparatively low this is cause due to the turbulence that is created due to increse the number of object in front of the shock tube and at exit object then wave gets of the shock tube.
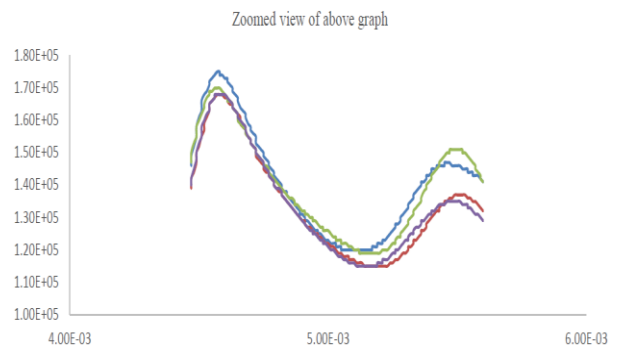
Figure.6. (b) Zoomed view of the above graph
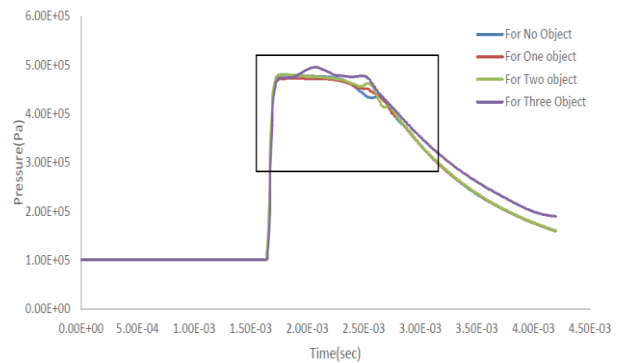
Figure.7. (a) Comparison of pressure distribution at 1.365m distance from shock tube when placing multi object at exitof shock tube.
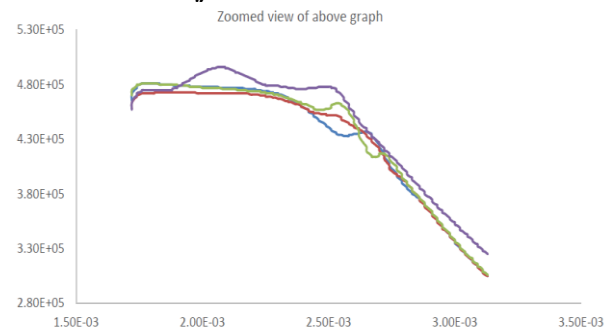
Figure.7. (b) Zoomed view of the above graph

At the conclusion of the experiment, the pressure was measured at the end of the shock tube along a vertical line extending from (X=2366 mm, Y=0 mm) to (X=2364 mm, Y=350 mm) at a rate of 4.15 milliseconds. This was done for each of the following scenarios: no objects, one object, two objects, and three objects. With the help of the data, we were able to determine that the pressure ratio of the diaphragm was 40. The decrease in wall pressure is due to the fact that the major vortices aren't lifting at that precise instant, as well as the fact that shock waves aren't being reflected. This study found that when the diaphragm to chamber pressure ratio is 40, the force of the blast on the wall is lower upstream of the shock tube exit but seven times the shock tube diameter when

11

confronting the wall. When the object approaches the wall, the blast load can be seven times the shock tube's diameter.

The blast load that is exerted on the wall is reduced as the distance rises (fig.). The picture demonstrates that the blast load on the wall will lessen when the object is placed further downstream of the shock tube exit, and that it will increase when the object will be travelling towards the wall at a pressure ratio of 40. The creation of a structure that is capable of mitigating the effects of blast waves will be beneficial. According to the information that was gathered, the peak pressure value on the item drops whenever the size of the object is made smaller, but it rises once the size of the object is made larger.

From the above zoomed view of the figure 6 (a) ,(b) and figure 7 (a) , (b) we can see the different curves of pressure variation with respect to time here we can that the peak pressure achieved on the wall is for no object and when we increase the number of object at exit of shock tube we can see that as the number of object gets decreases then gets decreases.

Based on my findings, I have concluded that the pressure/force generated by a shock tube depends on the object's size and its position within the tube; the larger the object, the greater the pressure/force generated, while the higher the object is within the tube and the closer it is to the tube, the faster the pressure/force will be generated. It has been noticed, as shown in figure, that when the pressure ratio increases, the peak pressure on the wall also increases. It also shows that when the pressure ratio rises, the pressure reaches its maximum value faster. To sum up, I found that when there is only one object, the blast wave is well mitigated, but when there are more objects, the wave is mitigated but still relatively low. This is because of the turbulence that is created when more objects are placed in front of the shock tube and at its exit

4. CONCLUSION

When we take a look at the simulation of the blast wave generation Using a piece of commercial CFD software called ANSYS Fluent, we were able to model both the pressure burst that came from the shock tube as well as its interaction with the wall. In order to tackle the problem of the transient flow, an implicit formulation of the second order was used, and the non-steady Navier-Stokes equations that involved compressible fluid were solved numerically in the form of an axi-symmetric system. The results of these two processes were then compared. These equations were coupled with the energy equation and the equation of state. In order to solve the convective terms, a Third Order MUSCL approach and an AUSM flux vector splitting scheme are utilised. T

he issue of blast load that is exerted on the wall as a direct consequence of the distribution of pressure has been researched for a number of different item sizes using a pressure ratio of 40 within the shock tube in order to gain a more in-depth understanding of the blast load that is exerted on the wall as a direct consequence of the distribution of pressure. This was done in order to get a better understanding of the blast load that is exerted on the wall as a direct consequence of the distribution of pressure.

According to the statistics, it is abundantly evident that relocating an object closer to the downstream end of the

shock tube exit would result in a reduced blast load, whereas moving it closer to the wall from the shock tube outlet would result in an increased blast burden. The opposite of this result would occur if the object were pushed closer to the wall from the outflow of the shock tube. The findings of this research have the potential to be exploited in the construction of architecture that provides higher protection against blast waves. This protection might potentially be achieved by using the findings.

Pressure, force varies with the size of the object in the shock tube and the position of the object, the higher the size of object, the greater the pressure, force created, and the higher the object is in the shock tube and more the object is near to the shock tube, the faster and more pressure, the force will be generated. The peak pressure value on the object is decreases if object size decreases and when increase the object size then peak pressure value on the object also increases.

5. FUTURE WORK

- Study an effect of blast load on object by placing it different position at exit of shock tube.
- The formation of shock wave, vortex ring and vortices due to interaction of blast with object will be study in near future.
- Based on this analysis the optimize distance from the exit of shock tube of the object can be calculated with the study in near future.
- The performance of a versatile shock tube that can be used to test different structural component at full or reduced scale.

REFERENCES

[1] Kundu Abhishek, Sudipta De, Murugan Thangadurai, C.L.Dora, Debopam Das, (2016) "Numerical visualization of shock tube-generated vortex–wall interaction using a fifth-order upwind scheme". Doi 10.1007/s12650-016-0362-x.

[2] Xavier, Sathish, (2011) "Numerical Analysis of Gun Barrel Pressure Blast Using Dynamic Mesh Adaption". Doi

[3] S. Dey, T. Murugan and D. Chatterjee, (2008) "Numerical Visualization of Blast Wave Interacting with Objects". Doi10.29252/jafm.11.05.28240.

[4] Anderson, J. D. *Computational Fluid Dynamics: the basics with applications*. McGraw-Hill, New York, USA.;1995.

[5] Arakeri, J. K., Das, D., Krothapalli, A. and Lourenco,L. Vortex ring formation at the open end of a shock tube: A particle image velocimetry study. *Physics of Fluids* 16(4), 1008-1019;2004. Doi 10.1063/1.1649339.

[6] Brouillette, M. and Hebert, C. Propagation and interaction of shock-generated vortices. *Fluid Dynamics Research* 21, 159- 169;1996. Doi 10.1063/1.870378.

[7] Jialing, J. E. (1999) Numerical Simulation of Shock (Blast) Wave Interaction with Bodies. Communications in Nonlinear Science & Numerical Simulation, 4(1). 1-7. Doi 10.1016/S1007-5704(99)90046-1.

[8] Takayama, F., Ishii, Y., Sakurai, A., Kambe, T. (1993) Self-Intensification in Shock Wave and Vortex Interaction. Fluid dynamic research, 12.343-348. Doi 10.1063/1.1388052

[9] Sun, M., Takayama, K. (2003) A note on numerical simulation of vertical structures in shock diffraction. Shock Waves 13 (1): 25–32. Doi 10.1016/j.compfluid.2005.05.001

[10] Takayama, K., Saito, T., Sun, M., Tamai, K., Tanno, H., Falcovitz, J. (2004). Unsteady drag force measurements of shock loaded bodies suspended in a vertical shock tube. Proceedings of the 21st International Congress of Theoretical and Applied Mechanics, Warsaw, Poland. Doi 10.1007/978-3-540-27009-6_153

[11] Murugan, T. (2008) Flow and acoustic characteristics of high Mach number vortex rings during evolution and wall interaction: An experimental investigation, PhD thesis, Indian Institute of Technology, Kanpur, India Doi 10.1063/5.0063164

[12] Murugan, T., Das, D. (2009) On the Evolution of Counter Rotating Vortex Ring Formed Ahead of a Compressible Vortex Ring. Journal of Visualization 12. 3.Doi 10.1007/BF03181934

[13] Murugan, T, and S. De (2012) Numerical visualization of counter rotating vortex ring formation ahead of shock tube generated vortex ring, Journal of Visualization, 15 (2): 97-100. Doi 10.1007/s12650-011-0110-1

[14] Murugan, T., and Das, D., Experimental Study on a Compressible Vortex Ring in Collision with a Wall. Journal of Visualization 15 (4), 2012, 321–332. Doi 10.1007/s12650-012-0138-x

[15] Murugan, T., De S., Sreevatsa, A., Dutta S. (2016) Numerical Simulation of Compressible Vortex - Wall Interaction, Shockwaves. 26 (3): 311–326. Doi 10.1007/s00193-015-0611-2

[16] Murugan, T., Sudipta, De, Dora, C. L., Das, D., (2018) A comparative three-dimensional study of impulsive flow emanating from a shock tube for shock Mach number 1.6.Journal of Visualization. Doi 10.1007/s12650-018-0503-5

[17] Kontis, K., An, R., Edwards, J. A. (2006) Compressible vortex-ring studies with a number of generic body configurations. The American Institute of Aeronautics and Astronautics (AIAA) 44. 2962-2978. Doi 10.2514/1.21018

[18] Kontis, K., An, R., Zare-Behtash, H., Kounadis, D. (2008) Head-on collision of shock wave induced vortices with solid and perforated walls. Physics of Fluids 20. 016104. Doi 10.1063/1.2837172

[19] Minota, T. (1993) Interaction of Shock with High Speed Vortex Ring. Fluid Dynamics Research, 12. 335- 342. Murugan, T., and Das, D. (2007) Experimental Investigation of the Acoustic Characteristics of Shock-Vortex Ring Interaction Process.13th AIAA/CEAS Aero acoustics Conference, 21-23, Rome, Italy. Doi 10.2514/6.2007-3422

[20] De, S. and Murugan T. (2011) Numerical simulation of shock tube generated vortex: effect of numeric. International Journal of Computational Fluid Dynamics 345–354. Doi 10.1080/10618562.2011.600694

[21] J. Jialing, "Numerical Simulation of Shock (Blast) Wave Interaction with Bodies" (1999) Chandra, Ganpule, Kleinschmit, (2012) "Evolution of blast wave profiles in simulated air blasts: experiment and computational modeling". Doi 10.1007/s00193-012-0399-2

[22] K. Kontis, R. Edwards, (2016) "Compressible vortex-ring studies with a number of generic body configurations".Doi 10.2514/1.21018

Preparation and UV Detection Characteristics of Graphene Oxide-ZnO Nanocomposite Thin Films

Shashank Dubey[a*],Sandip Kumar Singh[b],Himanshu Tiwari[a], Subodh Kumar[a], Ankush Gaurav[a]

[a]*Assistant Professor, Department of Mechanical Engineering, Uma NathSingh Institute of Engineering &Technology, V.B.S. Purvanchal University,Jaunpur, Uttar Pradesh, India. 222003*
[b]*Professor, Department of Mechanical Engineering, Uma NathSingh Institute of Engineering &Technology, V.B.S. Purvanchal University, Jaunpur, Uttar Pradesh, India. 222003*

* Email: shashank.dubey001@gmail.com

ABSTRACT

The quest for new materials in the area of optical electronics has had a significant impact on research into the development of nanocomposite materials with specific properties. In this study, graphene oxide-zinc oxide (GO-ZnO) nanocomposite thin films are produced and comprehensively studied in preparation for their application in UV detection. The typical combination of zinc oxide and graphene oxide allows for the synergistic use of the exceptional electrical and optical properties of both materials. TherGO-ZnO nanocomposite thin films were produced utilizing a straightforward and scalable solution-based technique that used a controlled chemical synthesis procedure. According to the structural and morphological analysis, the ZnO matrix and the graphene oxide sheets were successfully merged, keeping the homogeneity and crystallinity of the film. SEM and X-ray diffraction (XRD) were also employed to confirm the nanocomposite's surface characteristics and structural soundness. The GO-ZnO nanocomposite thin films' UV detection ability was thoroughly examined. In comparison to pure ZnO sheets, the photodetector devices showed dramatically improved photocurrent responsiveness and good UV radiation sensitivity. Additionally, the exceptional stability and repeatability of the nanocomposite during prolonged exposure to UV radiation highlight its potential for useful applications in UV sensing and photo detectionsystems.

Keywords: graphene oxide, zinc oxide, nanocomposite, thin films, uv detection, photodetector, optoelectronics.

1. INTRODUCTION

In the rapidly expanding fields of modern electronics and optoelectronics, the hunt for materials with remarkable electrical and optical properties has become essential. A single sheet of graphene is made up of a two-dimensional honeycomb lattice of carbon atoms. It has exceptional flexibility, mechanical strength, and electrical conductivity. The wide-bandgap semiconductor zinc oxide (ZnO), on the other hand, is renowned for its remarkable optical characteristics due to its high UV absorption and good transparency in the visible spectrum [1]. Combining the unique properties of graphene and ZnO inside a nanocomposite framework promises the development of novel materials that surpass their component components [2]- [4].The interaction between graphene and ZnO in nanocomposite systems has garnered a lot of interest recently due to the potential for concurrently harnessing the excellent electrical and optical capabilities of both materials [5]. The readily synthesized and functionalizable graphene oxide (GO), a derivative of graphene, has a variety of advantages. ZnO thin films optoelectronic capabilities can be enhanced by adding GO as a potential matrix, notably in the field of UV photo detection [6]- [8] For UV-based applications to fully realize their promise, high-performance UV sensors with improved sensitivity, rapid response, and exceptional stability must be developed. Photoluminescence. Due to their adjustable p-type photoluminescence, nanocomposite materials have become intriguing options for UV photodetectors in this context [9]. The primary subjects of this work are the synthesis and characterization of thin films constructed of graphene oxide-ZnO (GO-ZnO) nanocomposite materials, with a focus on the materials' UV detection characteristics [10]- [13]. By combining the unique properties of GO and ZnO, these nanocomposite films have the potential to provide better UV photo detection capability. This work aims to shed light on the structural, morphological, and electrical characteristics of GO-ZnO nanocomposites in order to comprehend the mechanisms underlying the enhanced UV sensitivity of these materials.

2. CHEMICALS AND MATERIALS

Graphene oxide (GO) was created using graphite flakes (325 mesh size, obtained from Alfa Aesar). The following chemicals were purchased from Alpha Aesar and utilized as received: sulphuric acid (H_2SO_4, 98%), potassium permanganate ($KMnO_4$, 99.9%), hydrogen peroxide (H_2O_2, 30%), $NaNO_3$, and ZnO. Alpha Aesar provided aluminum powder, which was purchased and applied as supplied. Throughout the sample preparation, distilled water and ethanol were employed.

2.1 Synthesis

The process of making graphene from graphene oxide generally involves the following steps:
1. Graphene oxide preparation: Graphene oxide was typically prepared by the graphite(1g) oxidation mixed with 0.5g $NaNO_3$ using a strong oxidizing agent such as potassium permanganate (3g very slowly)mixed with 25 ml concentrated H_2SO_4. This process

introduces oxygen-containing functional groups onto the surface of graphene, making it hydrophilic. The mixture was stirred for 1.3 h in an ice bath after stirring 140ml of DI water and 7 ml of H_2O_2 was added in the beaker solution and stirred for 2.5h.

2. Reduction of graphene oxide: In order to successfully get removal of the functional groups that contain oxygen and restore graphene's sp2 carbon-carbon bonding, graphene oxide must be reduced. This may be done by combining graphene oxide with a reducing agent (sodium borohydride, 2g), which are then combined in ethanol, a solvent. To make sure the graphene oxide is evenly distributed, the liquid is next agitated. The mixture is heated, typically at temperatures between 70°C to 100°C, to initiate the reduction reaction

3. Exfoliation of graphene:The reduced graphene oxide can then be mechanically sheared for two hours, mechanically stirred to separate the graphene oxide flakes, and then the resultant graphene sheets can be dispersed into a solvent.

4. Purification of graphene:Impurities such persisting oxidizing chemicals, unprocessed graphene oxide, or metallic catalysts utilized during production may be present in the graphene sheets. As a result, the produced graphene needs to be repeatedly washed with ethanol and DI water, then filtered and heated at 70°C.
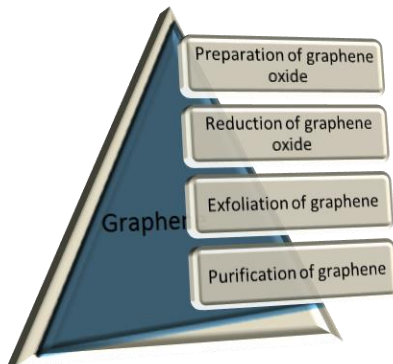
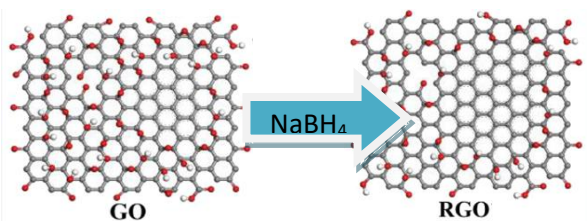

Figure.1. Process of making graphene

Figure.2. Reduction of GO to graphene
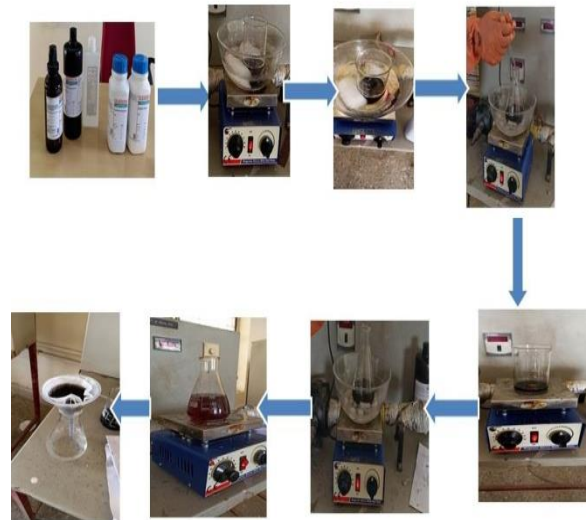
Figure.3. Illustration of detailed processing of rGO

Fabrication of ZnO-RGO composite In this study, ZnO-xRGO nanocomposite materials in various proportions (where x=1%wt and 1.5%wt) were prepared using powder metallurgical procedures. To eliminate impurities, the samples were further dried at 80^0C for 12 hours after being combined with 1%wt and 1.5%wt reduced graphene oxide powder and ZnOpowder in a ball mill at ambient temperature for 5 hours.
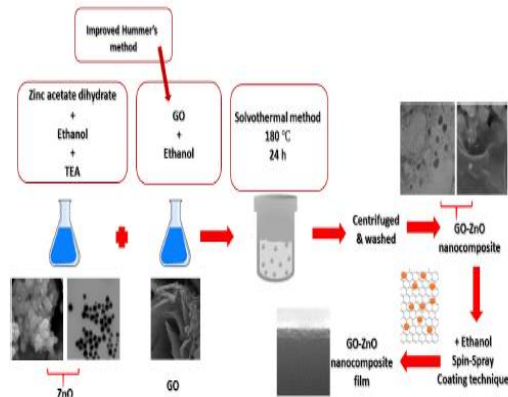
Figure.4. Process for synthesis of GZnO nanocomposite

3. RESULTS & DISCUSSIONS

Figs.5a show the Scanning electron microscopy (SEM) of pure grapheme which is prepared by the modified hummers method, Figs. 5 b &c shows the morphology structure of RZnO composite material powders in different proportions of graphene(1% & 1.5%wt) after the ball milling process. In the composite, RGO sheets are found on ZnO powder particles. The surfaces of the ZnO powders are covered with coiled and wrinkled RGO sheets, as seen in the enlarged SEM image. This outcome may result in the effective graphene in zinc oxide reinforcing action. The distribution of the reinforcement phase on ZnOl particles was seen in the SEM images of AMC powders reinforced with FLG sheets. But very little evidence of FLG sheets adhering to ZnOl particles has been found, and FLG sheets

have often been used in conjunction with ZnO powders.
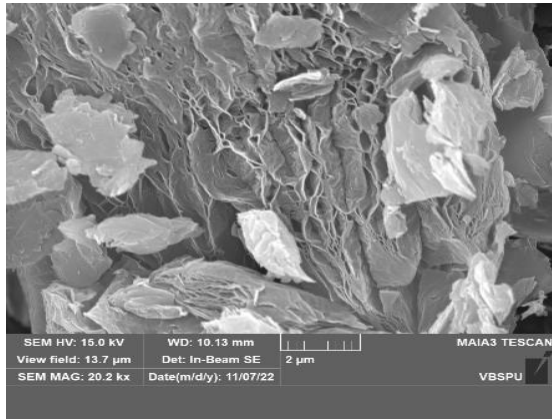
(a)
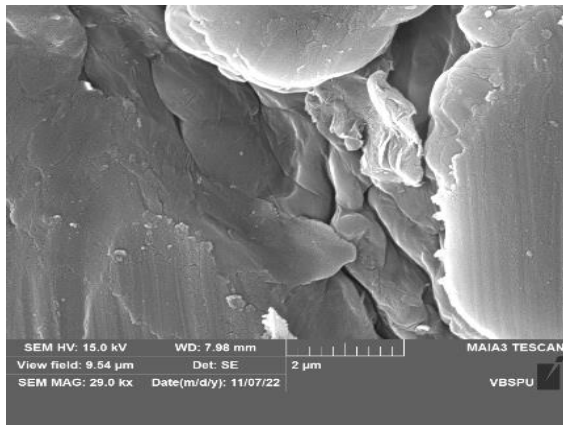
(b)
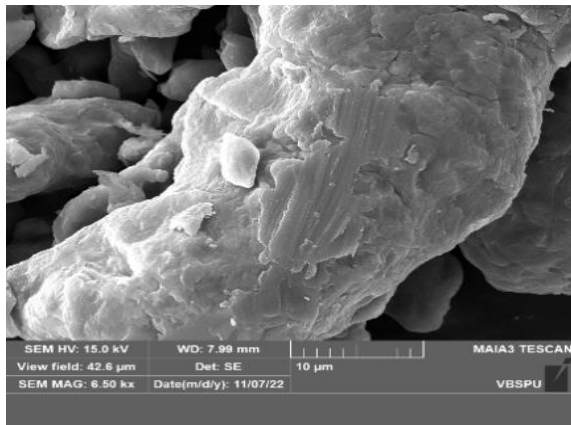
(c)

Figure.5. SEM images of graphene and GZnO composite

UV-VIS absorption spectra of graphene oxide (GO) (black), zinc oxide (ZnO) nanoparticles (pink), and ZnO/GO ratios of 1:1 (blue), 1:5 (amber), and 1:25 (red). There was water in every solution.
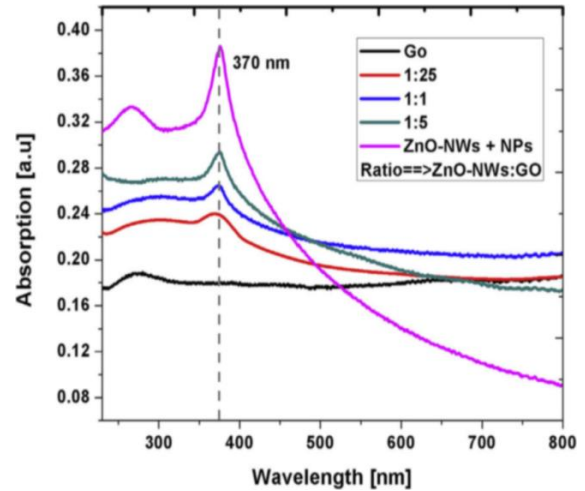
Figure.6. UV-visible absorption spectrum of reduced graphene oxide-ZnO nanocomposite thin film

4. CONCLUSIONS

In this study, GO was created utilizing a streamlined version of the Hummers process and developed as a low-cost, easy-to-use, and environmentally responsible way to create various RGO-based nanocomposites, including ZnO graphene nanocomposite material.

SEM and UV Vis were used to examine and successfully describe the sample. The SEM findings imply that the graphene nanoparticles in the ZnO metal oxide matrix are distributed uniformly. The prior literature also supports the particle sizes found in these observations.

In conclusion, mechanical stirring was used to create ZnO-graphene composites. Based on the SEM and UV Vis results, it is hypothesized that uniform mixtures of RGO between the ZnO particles were obtained such that there were no significant agglomerates, demonstrating that the mechanical mixing method using the ball and the powder in an aqueous dispersion was effective in producing the composite powder with good homogeneity and no oxidation.

REFERENCES

[1] Wang, B. *et al.* Graphene-based composites for electrochemical energy storage. *Energy Storage Mater.* 24, 22–51 (2020).

[2] Wang, J. *et al.* Effect of the graphene content on the microstructures and properties of graphene/aluminum composites. *New Carbon Mater.* 34, 275–285 (2019).

[3] Saboori, A., Moheimani, S., Pavese, M., Badini, C. & Fino, P. New Nanocomposite Materials with Improved Mechanical Strength and Tailored Coefficient of Thermal Expansion for Electro-Packaging Applications. *Metals (Basel).* 7, 536 (2017).

[4] Tjong, S. Microstructural and mechanical characteristics of in situ metal matrix composites. *Mater. Sci. Eng. R Reports* 29, 49–113 (2000).

[5] Liao, Z. *et al.* State-of-the-art of surface integrity in machining of metal matrix composites. *Int. J. Mach. Tools Manuf.* 143, 63–91 (2019).

[6] Ma, Z. ., Tjong, S. . & Wang, Z. . Cyclic and static creep behavior of Al–Cu alloy composite reinforced with in-situ Al2O3 and TiB2 particulates. *Mater. Sci. Eng. A* 264, 177–187 (1999).

[7] Tjong, S. Abrasion resistance of stainless-steel composites reinforced with hard TiB2 particles. *Compos. Sci. Technol.* 60, 1141–1146 (2000).

[8] Bai, G. *et al.* Tunable coefficient of thermal expansion of Cu-B/diamond composites prepared by gas pressure infiltration. *J. Alloys Compd.* 794, 473–481 (2019).

[9] Dorri Moghadam, A. *et al.* Functional Metal Matrix Composites: Self-lubricating, Self-healing, and Nanocomposites-An Outlook. *JOM* 66, 872–881 (2014).

[10] SABOORI, A., CHEN, X., BADINI, C., FINO, P. & PAVESE, M. Reactive spontaneous infiltration of Al-activated TiO2 by molten aluminum. *Trans. Nonferrous Met. Soc. China* 29, 657–666 (2019).

[11] Salur, E., Aslan, A., Kuntoglu, M., Gunes, A. & Sahin, O. S. Experimental study and analysis of machinability characteristics of metal matrix composites during drilling. *Compos. Part B Eng.* 166, 401–413 (2019).

[12] Liu, L., Li, W., Tang, Y., Shen, B. & Hu, W. Friction and wear properties of short carbon fiber reinforced aluminum matrix composites. *Wear* 266, 733–738 (2009).

[13] Moustafa, S. ., El-Badry, S. ., Sanad, A. . & Kieback, B. Friction and wear of copper–graphite composites made with Cu-coated and uncoated graphite powders. *Wear* 253, 699–710 (2002).

Dynamic analysis of a Point-Absorber for Indian Off-shore Sea Conditions

Sai Ram Baradwaj[a]* Sanjeev Kumar Arya[b]

[a] *Department of Applied Mechanics, Motilal Nehru National Institute of Technology, Allahabad, Prayagraj, 211004, India*
[b] *Department of Civil Engineering Rajshree Institute of Management and Technology, Bareilly U.P, India*

*E-mail ID: bdevanuru@gmail.com

ABSTRACT

This study focused on a two-body point absorber-based wave energy converter that extracts energy from the water by drifting up and down with the wave motion. Then ovel geometry of a two-body point absorbers has been used to carried out static and transient structural analysis.The time varying load are applied on the system, all of which are analysed thoroughly for von-mises stress and total deformation. Acceptable results were obtained for most of the components.

Keywords: Point absorber, hydro dynamic force, ansys, steel and aluminium properties

1. INTRODUCTION

As fossil fuel sources run out and the need for energy rises, several nations are putting significant effort into developing renewable energy resources. There are, however, other reasons to think about putting more focus on creating renewable energy sources, not only environmentalists but People in general are more and more aware that consuming fossil fuels and releasing pollutants into the environment contribute to warming our planet, the effects of which are currently being addressed on a global scale.

To have significant effects on the green energy environment, all prospective resources must be explored and developed [1]. Compared to wave energy, solar and wind energies have so far drawn a lot of attention. When compared to other energy sources like as wind and solar energy, the energy from waves has a higher energy density contains 2–3 kW/m^2 of per unit volume of energy while wind and solar contain 0.5 kW/m^{2}and 0.1–0.3 kW/m^{2}per unit volume of energy respectively [2].This high energy density seems to have the potential to harvest electricity with better efficiency when compared to other techniques of renewable energy. Two-thirds of the earth is covered with water, with intermittent waves that are a potential form of energy just waiting to be harnessed [2].The device responsible for capturing and converting wave energy is the wave energy converters (WECs). There are three basic ways to harvest wave energy

Oscillating water columns: Waves move upwards and downwards vertically to create water or air pressure that can be used to power a turbine.

Oscillating body systems: The wave created rolling, pitching, or heaving of a body that floated, which was used to operate the turbine via cams or shafts.

Overtopping converters: The pressure generated by the concentrating of waves into a narrowing channel is used to rotate the turbine.

The oscillating body kinds of WEC, or point absorbers, are the subject of this paper. By this definition, point absorbers have capture widths that are much shorter than the wavelength of the incoming wave and behave largely in heave motion.

The device possesses wave orientation independence and is able to absorb energy from any and all wave degrees due to its small form, even if wave directions can change significantly over the course of the device's lifecycle [4]. The advantages of this technology also include simple production and implementation. However, because of nature's unpredictable nature, harsh sea conditions, particularly during storms, unusual sea states, where extremely powerful waves with extreme heights and forces are getting excited on the WEC, put many of structural and survivability inquiries, resulting in significant uncertainties in environmental burdens, making their evaluation of structure very challenging [5]. The organizations of this paper are 3-D model of the geometry has been created in the design module of ansys commercial software. Structural meshing of the corresponding body is generated in meshing module using various meshing parameters [6]. Grid independency test has been carried out in ansys static structural module corresponding to maximum von mises stress [7]. Transient structural analysis of the point absorber has been carried out to obtain total deformation and stresses.
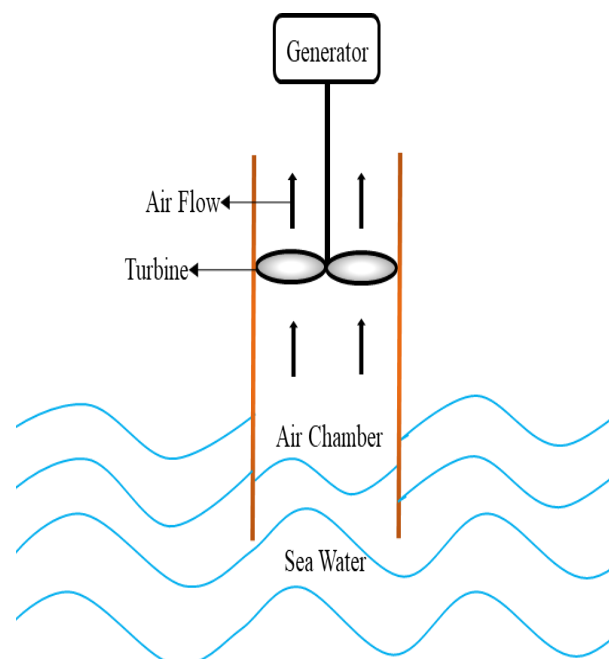
(a) Oscillating Water column
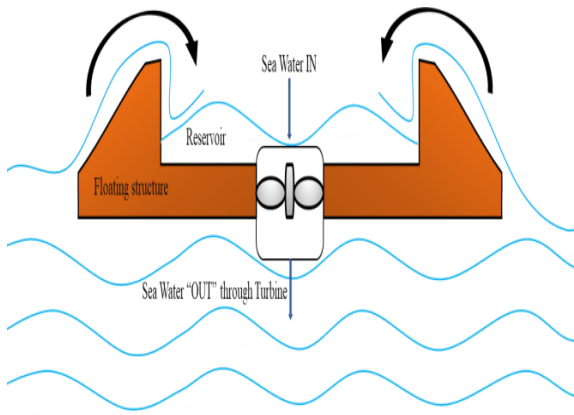
(b) Overtopping
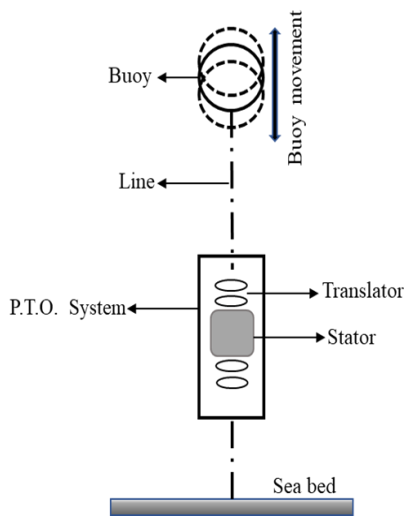
(c) Oscillating body

Figure.1. Schematic representation of the various wave energy technologies

2. METHODOLOGY

2.1.Engineering material

The buoy and plate stiffener of the novel geometry is being simulated with different types of materials like steel and aluminium. Therefore, in this study, the Steel and aluminum, which is Steel frequently used for offshore structures, are considered to be the materials for the buoy and plate. Table 1 shows the mechanical characteristics of steel and aluminum, whereas Table 2 lists the geometry characteristics.

Table 1: Material Properties

Material	Density(Kg/m³)	Modulus of elasticity	Poisson ratio	Tensile yield strength	Compressive Yield Strength
Structural steel	7850	200GPa	0.3	250MPa	250 MPa
Aluminium	2770	70GPa	0.34	280MPa	280 MPa

2.2 Geometry

Table.2.Geometry properties

Bodies	Centroid X(m)	Centroid Y(m)	Centroid Z(m)
Buoy	0	0	12.3
Plate	0	0	0.43
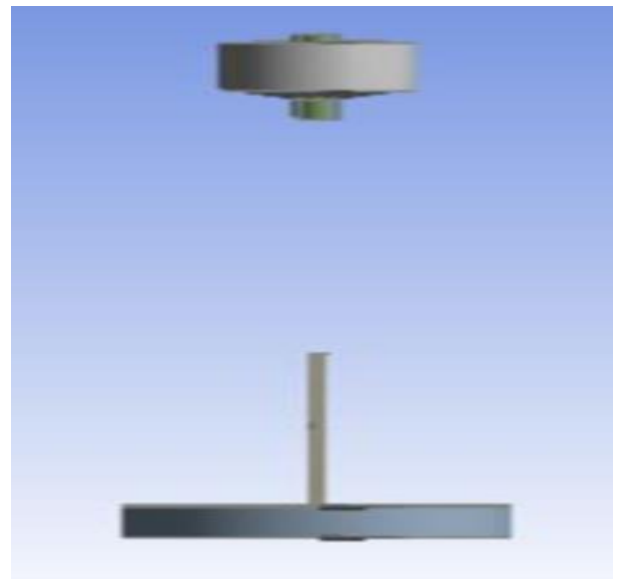
(a) Two-body PA
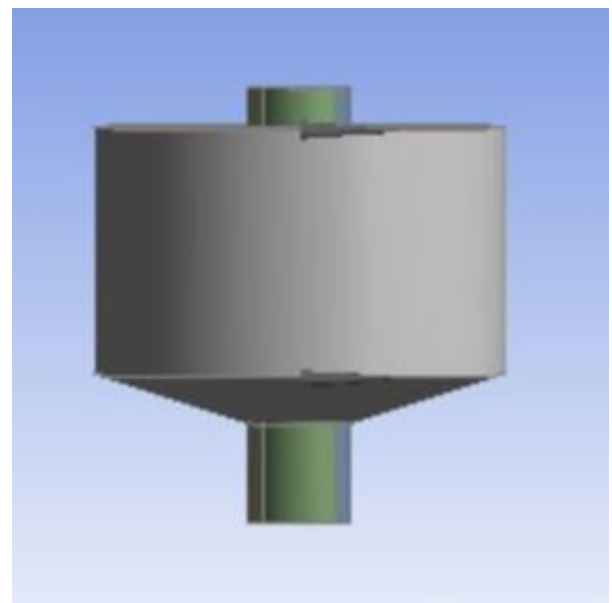
(b) Buoy
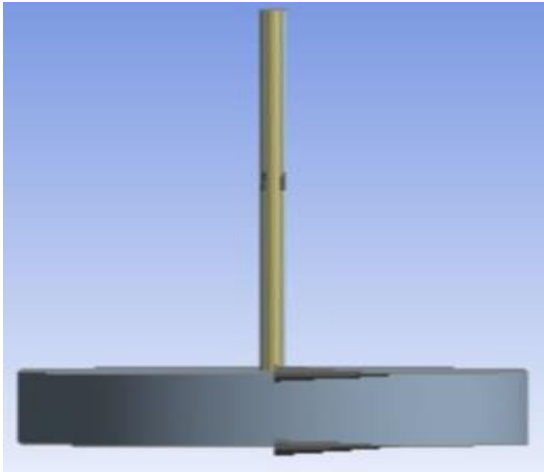
(c) Plate

Figure.3. 3-D model of point absorber

2.3 Meshing

3-D modeled has been divided into small parts in design module of ANSYS commercial software to generate the structured mesh. The required mesh size is defined and various steps are performed to produce a mesh of high quality. Grid angles are exceptionally good, mesh sizes transition smoothly, and high aspect-ratio elements are generated. In addition, high stress region and edges are further refined.
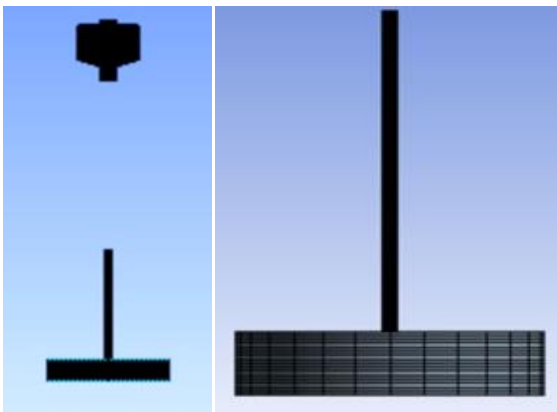
(a) Two-body PA   (b)   Buoy

(c) Plate

Figure.4. Meshing of two-body PA

2.4 Boundary condition

Hydrodynamic force has been calculated from Hydrodynamic-Diffraction analysis, has been used to perform the analysis [1]the change in hydrodynamic load with the duration of the wave energy converter, where maximum value of excitation forces for the buoy is 8.78kN/m and for the reaction plate is 85.72kN/m. For grid independent analysis, maximum force is applied on the buoy and plate respectively to find the von mises stress. In this problem, force is varying with time so transient structural analysis has been done. In analysis setting the time steps is auto programmed for time of 3sec to 12sec. Calculated forces has been applied at CoG using remote force conditions of conical buoy and plate stiffener. Bodies are constrained using remote displacement boundary conditions for fixing the rotation of the body. In solution setup, total deformation tool and stress tool are applied to calculate total deformation and stress in the body respectively.

Software tools are used for the simulation work. Computational domain is two-dimensional. Geometry is designed using the Design Modular. The driver's section is 165mm long and the driven segment is 1200mm long. Diameter of the shock tube is 64mm. The shock tube exit is into the rectangular box of size 1000mm × 600mm. As the shock tube's shape is uniform about the axis that is horizontal, only half of it is simulated to reduce computational time. Meshing is done using the meshing tool available in the ANSYS workbench. Minimum orthogonal quality of the mesh is 0.999988, maximum orthogonal skew is 1.72853e-06 and maximum aspect ratio is 19.63. There are a total of 175,000 parts, and there are a total of 176451 nodes. Solver is density based. Pressure in the driver section is 4000000 Pa. and 101325 Pa. in the driven section. All boundaries except the axis are takenas wall.

Figure.5. Loads applied on the body
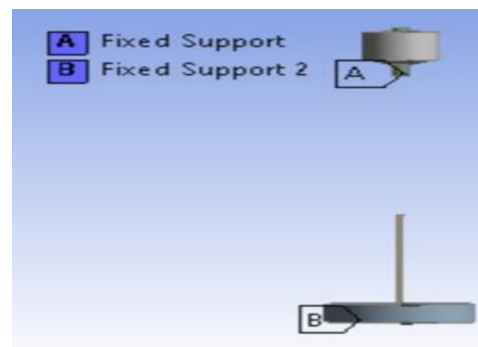
Figure.6. Supports applied to the body

3. RESULTS & DISCUSSION

3.1. Grid independent test

Grid independence was conducted on four meshes in ANSYS Structural module. Very negligible difference is observed by improving the mesh cells from 402050 to 50,698. This grid independence test was conducted corresponding to max von mises stress. So, the grid size of 402050 is considered as optimum mesh size.

3.2. Governing equation

The Navier-Stokes equations regulate CFD. It relies on the physical properties of the fluid conservation law. For explosion wave simulations, the continuity equation, energy conservation equation, equation of state, momentum

(a)   (b)

Figure.8. Deformation at water surface level when aluminum is used

GRID INDEPEDENCY TEST

Figure.7. Grid independent Study graph in static structural analysis.

3.3. Results

The transient structural analysis of the 2-boby point absorbers has been carried out using two different materials which are available in ANSYS commercial software package. The stiffener plate has undergone max defamation of 0.06m under the time varying load as shown in fig 8 and fig9. Whereas, for buoy max deformation is happening at water surface level when aluminum is used as shown in fig 10 and for material of structural steel the deformation in negligible shown in fig 11

(a)   (b)

Figure.9. Deformation at water surface level when structural steel is used
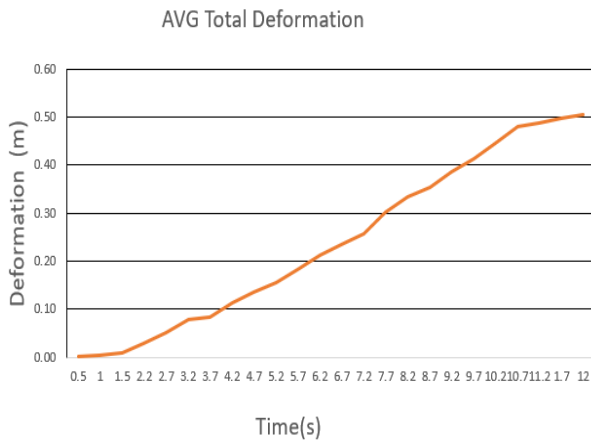
Figure.10. Deformation of point absorber over applied force for aluminum
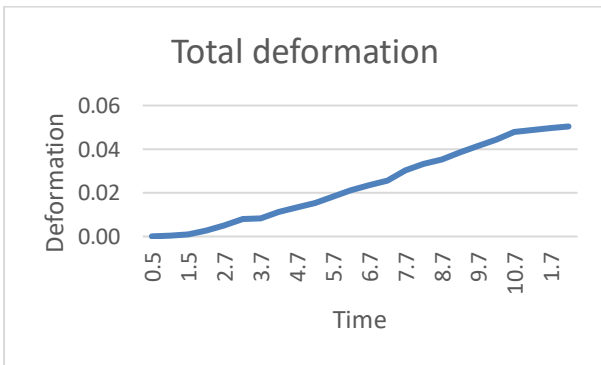
Figure.11. Deformation of 2-body point absorber over applied force

4. CONCLUSION

The focuses of recent research work on the static and transient structural analysis of the 2-body point absorber system for Indian offshore conditions. The stress and deformations found are with respect to time varying Froude-Krylov and diffraction force. To obtain the accurate deformation of two body point absorber Fluid-Structure Interaction needs to be performed. Additional observations are needed because consideration must be given to the harsh environments expected in offshore conditions, which cannot be completely replicated with simulation.

REFERENCES

[1]   Singh, D., Singh, A., Paul, A.R. and Samad, A., 2021. Design and simulation of point absorber wave energy converter. In E3S Web of Conferences (Vol. 321, p. 03003). EDP Sciences.

[2]   Ocean Waves and Oscillating Systems Linear Interactions Including Wave-Energy Extraction by Johannes Falnes.

[3]   Arief, I.S., Utama, I.K.A.P., Hantoro, R., Prananda, J. and Megawan, A.M., CFD Simulation for Designing Mooring Bitts Position at the Barge for Wave Energy Conversion (WEC).

[4]   Bucchi, A. and Hearn, G.E., 2016. Analysis of the SEA-OWC-Clam wave energy device part B: Structural integrity analysis. Renewable Energy, 99, pp.253-269.

[5]   Kolios, A., Di Maio, L.F., Wang, L., Cui, L. and Sheng, Q., 2018. Reliability assessment of point-absorber wave energy converters. Ocean Engineering, 163, pp.40-50.

[6]   Beirao, P.J.B.F.N. and Malça, C.M.D.S.P., 2014. Design and analysis of buoy geometries for a wave energy converter. International Journal of Energy and Environmental Engineering, 5(2), pp.1-11.

[7]   Al Shami, E., Zhang, R. and Wang, X., 2019. Point absorber wave energy harvesters: A review of recent developments. Energies, 12(1), p.47.

[8]   Van Rij, J., Yu, Y.H. and Guo, Y., 2017, June. Structural loads analysis for wave energy converters. International Conference on Offshore Mechanics and Arctic Engineering (Vol. 57786, p. V010T09A023). American Society of Mechanical Engineers.

Heat transfer Augmentation Using Metal Foam

Upendra[a], Sanjeev Kumar Arya[a*]

[a]Department of Applied Mechanics, Motilal Nehru National Institute of Technology Allahabad, Prayagraj, 211004, India

*E-mail ID : aryaaryan551@gmail.com

ABSTRACT

In this present research the heat transfer and flow behaviors of horizontal cylinder in forced convection flow over bounded with "whole and segmented porous layer" of metal foam are studied. Different-different porosity and pore density of metal foam layer are tested. The horizontal cylinder is heated with constant temperature and forced convection are tested for Re no. range of 8000-19000. In this study two configuration are tested one is for complete porous layer of constant thickness of 1.5 diameter ratio and another is for segmented porous layer of same thickness i.e., 1.5 diameter ratio, in segmented porous layer one part is attached at 0^0 incident angle and another part is attached at the rear. The coefficient of heat transfer and drag are calculated in to determine the "thermal enhancement performance" which relates the augmentation in heat transfer with pressure drop. In case of whole porous layer this provides However, the segmented metal foam case at 0^0 incident angle gives best performance with lower pressure drop, signifying he best thermal enhancement factor.best result as compare to both the case i.e., bare case and segmented porous case but with higher pressure drop.

Key words: forced convection, heat transfer augmentation, and segmented, metal foam.

1. INTRODUCTION:

Utilizing metal foams on the flow channel, especially in tiny heat exchangers, is a relatively innovative method for enhancing heat transfer from cross flowing cylinders. Metal foams are great candidates for improving the heat exchange between the surface and the flowing fluid due to their high thermal conductivity and tortuous paths that cause turbulent flows of air passing through the porous zone. Due to the significant pressure loss, using metal foams needs an increase in pumping power to accelerate the flow through them.

The usage of non-renewable fuels is afflicted by a high rate of thermal energy waste, which may be more effectively stored and utilized. There are a number of manufacturing applications where energy transmission is necessary, including air conditioning systems, refrigeration, and automotive radiators. It has been a lengthy but still necessary sector in our everyday lives, especially with the increasing usage of miniaturised technological devices. Heat resources and operating expenses might be saved enormously by improving thermal energy transfer efficiency. The ancient yet effective method of transferring energy from a hot face by impingement gas jet cooling is still commonly employed today. The cooling method of jet impingement is utilised for a variety of systems, such as turbine blades and electronic devices that need cooling. Hueng et. al. (2007) said that the performance parameter heat exchanger with rise in pressure drop.

Odabaee et. al. (2011) reported that hoe heat is transferred from a cylinder placed in packed bed in forced convection; they said that heat transfer coefficient increases with smaller in particle size. Leong et. al. (2011) investigated in graphite foam with baffled and staggered to overcome loss in pressure drop with more heat transfer. Chumpia et. al. (2012) investigated that efficient brazing process can be reason to increase heat transfer rate

Layeghi et. al. (2019) analysed heat transfer from set of tube in direct contact type and concluded that there is 80 % increase in heat transfer in case of metal foam.

Saivashi et. al. (2018) investigated for variable porosity and multi layered foam and concluded that maintaining a constant low pore structure at various porosity improves performance, also adding a little amount of nano fluid to the flow increases performances by 5 %.

Bhattacharya et. al. (2008) investigated the enhancement of heat transfer over different-different foam film width and concluded that over certain foam thickness heat flow reaches asymptotically. Odabaee et. al. (2011) demonstrated that after the first fourth of tube local Nusselt number reaches a maximum that gives idea to use metal foam in form of segmented. Wang et. al. (2014)they done for thin thickness of foam of 1.3 diameter ratio at large porosity with low PPI and concluded that heat transfer enhanced by 18 times at Re 6000.

Alvandifar et. al. (2018)used segmented metal foam and concluded that covers half of the cylinder reduce pressure drop by 60 % and 33 % increase in area goodness factor.

Al-Sumaily et. al. (2014)studied effect of putting tube bank inside a porous layer in various structure and concluded adding metal foam enhance thermal efficiency.

Du et. al. (2010) and Xu et. al. (2014) studied analytically parallel and counter flow heat exchanger to increase of effectiveness up to0.95 at porosity of 0.8. Odabaee et. al.(2012) and Wang et. al.(2017) explored the tube bank enclosed in aluminium foam layer of various thickness and result were outperform over finned type.

Huisseune et. al. (2015)examined metal foam as louvred and finned heat exchanger while using low pow PPI's such as 10 and 20 the pressure loss for louvred was slightly higher. Zhao et al. (2012) investigated heat transfer in porous metal foam for forced convection in single phase, flow boiling, and pool boiling heat transfer radiation, which resulted in the development of a compact heat exchanger. Boyd et al. (2012) used a 3D model to analyse the meta foam heat exchanger for different cooling techniques such as air and water cooling and concluded that the performance of an air-cooled metal foam heat exchanger for fuel cell applications with the same pressure drop is identical to that of a water-cooled heating

element. Lu et al. (2006) used the "Brinkman Extended Darcy flow model" and the "LTNE model" to conduct an analytical research of pipe-filled metal foam and determined that small pore size and low porosity play a key role in thermal performance. Jeng et. al. (2007) conducted numerical solution of parallel plate for various aspect ratios and concluded that the Nu no. was 20 times greater than in metal foam case than non-metal case. Boules et. al. (2021) conducted analytical and experimental for porous medium around the cylinder for different thickness of metal foam i.e., diameter ratio of 1.3 and 1.5, and the diameter ratio 1.5 gives better result as compare to 1.3 diameter ratio. Also calculated local Nusselt number around the cylinder, and found best setup for segmented metal foam i.e., at 0^0 incident angle give better result than other combination.

2. COMPUTATIONAL METHODOLOGY

In this paper, we talk about transfer of heat from a horizontal, constant wall of cylinder that is wrapped by a layer of metal foam.Boules et. al. (2021)the 2-D model has a tube with a diameter of D_b=38.1 mm and a perimeter temperature of T_w that stays the same, as well as a layer of metal foam with a diameter of "$D_f = 1.5 D_b$". The incoming forced flow into the computational domain has constant velocity V and temperature T as it travels over the horizontally positioned porous wrapped cylinder at the domain's centre, as shown in Figure. The outer boundary condition is taken as rectangular with length 20 times of cylinder dia. and width as 5" with a velocity inlet condition applied at the left face of the domain and the right face is defined as a pressure outlet.

For research purposes, different pore densities (PPI) of aluminium metal foam are investigated. The aluminium metal foams range in porosity from 0.90 to 0.97. According to Table 1, Bhattacharya et. al. (2002) provides the parameters of the metal foam considered for the current investigation also provides the uncertainty in the observed permeability values.

The domain is modelled under the following assumptions:

Natural convection, i.e., effects of gravity, and radiation heat transfer are negligible.

The thermo physical properties of the airis considered constant and temperature independent Table (2)

The metal foam is considered isotropic and homogeneous with uniform porosity. The material of the metal foam is Aluminium and the properties of the metal foam are listed in Table (1).

The arrangement condition is illustrated as a full porous layer around the cylinder, as previously demonstrated. Only a part of the metal foam is wrapped around the horizontal cylinder in the other design. The metal foam covers half of the cylinder's perimeter surface, leaving the other half accessible to incoming air. The metal foam itself is separated into two portions; one piece covered a portion of the cylinder's front side, while the other covered a portion of the cylinder's back side, as seen in the figure.

2.1. Grid Independence Study

To determine optimum grid for numerical calculation grid independent test is done for 5 PPI of aluminium metal foam with constant temperature of cylinder is considered. Detailed grid sensitivity studies for four distinct grid size of 7242, 9363, 14860, and 24860 are performed for segmented metal foam case. As after 14860 element size result output was constant so this element is taken for further calculation. Also, four case were simulated for whole porous case for 5 PPI of aluminium metal foam with same boundary condition and 12387 element was optimal grid after this result output was same for this case so this element is taken as optimal element size for whole porous case shoen in Figure 1 and Figure 2.

Table.1.Thermophysical property of the metal foam used Bhattacharya et al. (2002)

Property	PPI	Porosity (ε)	Permeability (K)x10^{-7} m^2	Forchheimer coefficient (C_F)	Ligament diameter d_f (m)	Pore diameter d_p (m)
Value	5	0.9726	2.7	0.097	0.0005	0.00402
	5	0.9118	1.8	0.085	0.00055	0.0038
	10	0.9138	1.1	0.07	0.00045	0.00328
	10	0.9486	1.2	0.097	0.0004	0.00313
	20	0.9546	1.3	0.093	0.0003	0.0027
	20	0.9005	0.9	0.088	0.00035	0.00258
	40	0.9132	0.53	0.084	0.00025	0.0018

Table 2: Property of air Boules et. al. (2021)

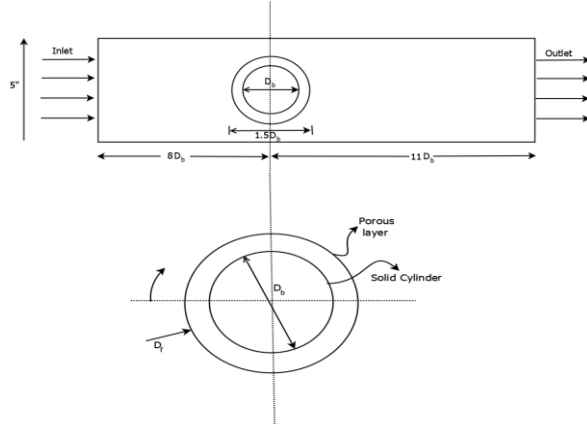| Property	Density	Viscosity	C_P	Thermal Conductivity
Value	1.225kg/m^3	1.7894 x 10^{-5} Kg/m-s	1006 J/kg-K	0.0242 W/m-K

Figure.1. The fluid region, as well as near view of the "whole porous layer case"
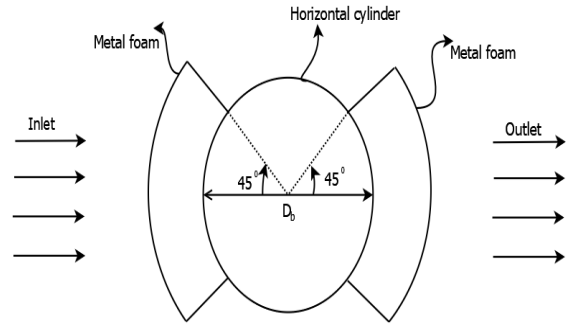

Figure.2. The fluid region, as well as near view of the "segmented porous layer case"

2.2. Equations

The domain of 2-D incompressible unsteady flow is divided into two regimes: the exterior domain and the porous region. Together, the Navier-Stokes and Darcy-Brinkman-Forchheimer equations regulate the flow field in the porous domain. The basic equations for the open region are the same as those for open pipe flow. In the mathematical model for the metal foam region, the effects of porosity, permeability, etc. are taken into account. These are the "Reynolds averaged Navier-Stokes" (RANS) equations:

Continuity equation:

$$\frac{\partial(\rho_f u_i)}{\partial x_i} = 0 \tag{1}$$

Momentum equations:

$$\frac{\partial(\rho_f u_i u_j)}{\partial x_j} = -\frac{\partial p}{\partial x_i} + \frac{\partial}{\partial x_j}\left(\left(\mu_f + \mu_t\right)\left(\frac{\partial u_i}{\partial x_j} + \frac{\partial u_j}{\partial x_i}\right)\right) + \rho_f g \beta\left(T - T_\infty\right) \tag{2}$$

Energy Equation:

$$\frac{\partial(\rho_f u_j T)}{\partial x_j} = \frac{\partial}{\partial x_j}\left(\left(\frac{\mu_f}{\Pr_f} + \frac{\mu_t}{\Pr_t}\right)\frac{\partial T}{\partial x_j}\right) \tag{3}$$

The effective qualities of the porous zone can be defined in a variety of ways, the most common of which is a weighted average computation.

$$\left(\rho C_P\right)_{eff} = \varepsilon\left(\rho C_P\right)_{fluid} + \left(1-\varepsilon\right)\left(\rho C_P\right)_{solid} \tag{4}$$

$$k_{eff} = \varepsilon k_{fluid} + \left(1-\varepsilon\right)k_{solid} \tag{7}$$

Based on the inflow stream velocity and the bare cylinder diameter, the Reynolds number is taken into account in the fluid domain.

$$\mathrm{Re}_D = \frac{\rho_{fluid} V_\infty D_b}{\mu_{fluid}} \tag{8}$$

Calculations of the Nusselt number (local and average) and $Nu_{avg}{}'$ are used to analyse the transfer of heat properties of a cylinder coated with a porous layer in unsteady flows.

$$Q^{"} = -k_{eff}\frac{\partial T}{\partial r}, \quad h_{loc} = \frac{Q^{"}}{\left(T_w - T_\infty\right)}$$

$$, \quad Nu_{loc} = \frac{h_{loc} D_b}{k_f} \tag{9}$$

$$Nu_{loc} = -\frac{k_{eff} D_b}{k_f\left(T_w - T_\infty\right)}\frac{\partial T}{\partial r}\bigg|_{r=Rb} \tag{10}$$

$$Nu_{avg}{}' = \frac{1}{2\pi}\int_0^{2\pi} Nu_{loc}\,d\theta \tag{11}$$

$$\overline{Nu} = \frac{h_\infty D_{bare}}{k_{air}} \tag{12}$$

2.3. Numerical Methods

On Ansys Fluent, the governing equations have been broken up into small pieces using the Finite Volume Method. To solve the flow field, a 2-dimensional, steady, double-precision, pressure-based solver was used. A coupled algorithm scheme is used to connect the speed and pressure fields. A second-order implicit scheme was used for the discretization of the time derivative term. The Gauss-Seidel nodal method was designed to solve algebraic equations in steps. The tolerance for residual errors in the dependent variables was set to order

of 10^{-5} .In the -direction, the flow domain was set up with a uniform structured grid. In the r-direction, the grid was skewed, with the smallest cell size near the wall of the bare cylinder and at the boundary between the porous and fluid zones, as shown in Figure 3 and figure 4.According to Bejan et al. (2017), the minimum cell size along the walls and the porous-fluid interface is substantially less than the porous region's boundary layer width, which is on the order of

$$\sqrt{K / \varepsilon} \, .$$

2.4. Validation:

The validation is done for both the where the average Nusselt number is calculated for different Reynolds number and then compared to previous result. The validation is comparing the result of analytical study of a whole and segmented porous layer over a horizontal cylinder done by; David Bouleset al., (2021) using porous zone properties ε=0.9, PPI=20, C.F.=0.075, K=0.975 x 10⁻⁷ for different Reynolds number.
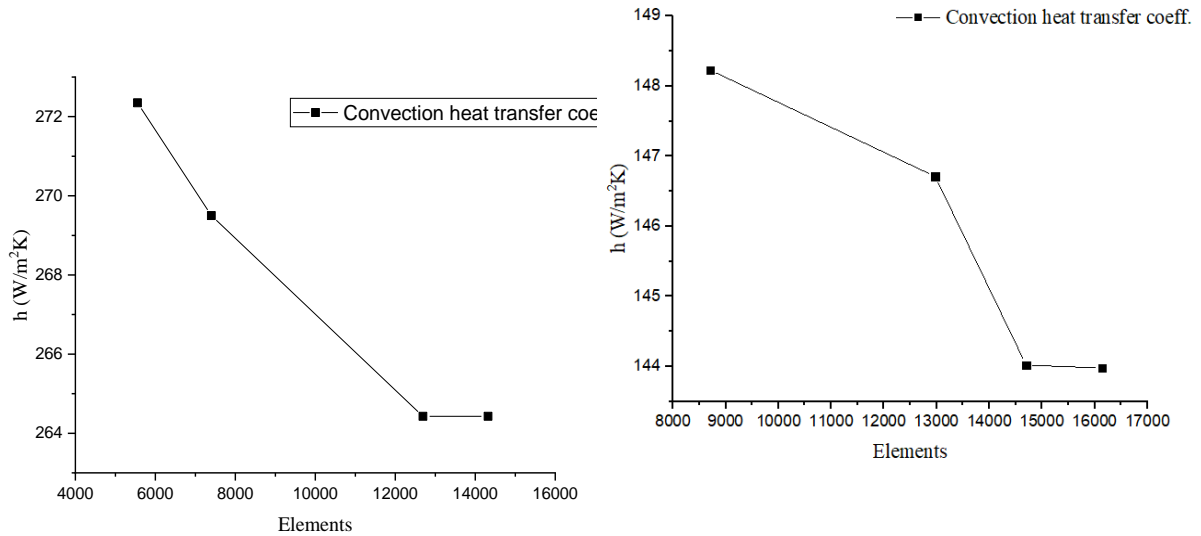

Figure.3. Mesh sensitivity analysis for "whole porous case and segmented porous case"
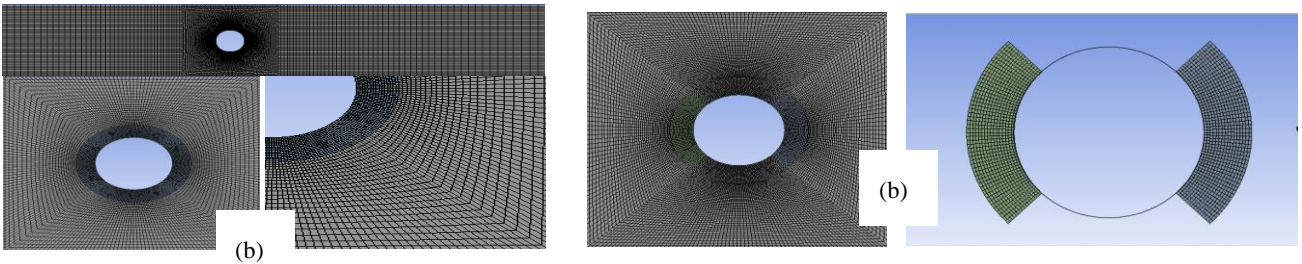
Figure.4. Mesh around the cylinder wall for "(a) whole and (b) segmented porous layer" case
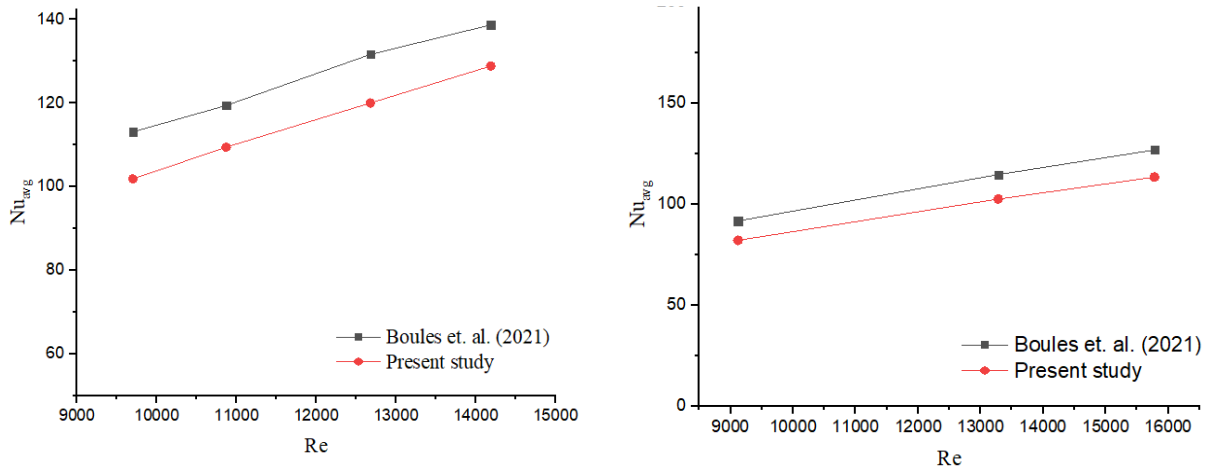
Figure.5. Validation of "forced convection" over a "(a) whole and (b) segmented porous layer" for the present analytical

26

Maximum error for the case whole porous case is 9 % and for segmented porous case is 9.5 %. The result of whole porous layer of analytical model against the study in this case is presents in the graph shown above in figure 5.

3. RESULTS & DISCUSSION

Effect of porous layer around cylinder for both cases i.e., whole and segmented porous layer case are investigated in terms of pressure drop heat transfer and drag coefficient. The entrance velocity of flow region varies in the range of Reynolds number of 8000-19000. The pressure, temperature and velocity contours for bare cylinder, whole and segmented porous case showed at Re of 17000 in figure 6, 7 & 8

the flow through the porous layer on the front side is accelerated.

3.1. Heat transfer enhancement

Figure 8 & 10 shows the Nu no. for the entire and segmented porous layer, with the parameters of the porous zone listed in Table (1). The impact of the enhanced heat transmission is represented by the ratio ("Nu_f/Nu_b") of the Nusselt number in the whole porous cylinder case to the Nusselt number in the cylinder case without pores. The cylinder, porous and segmented porous layer examples are conducted at Re values between 8000 and 19000.
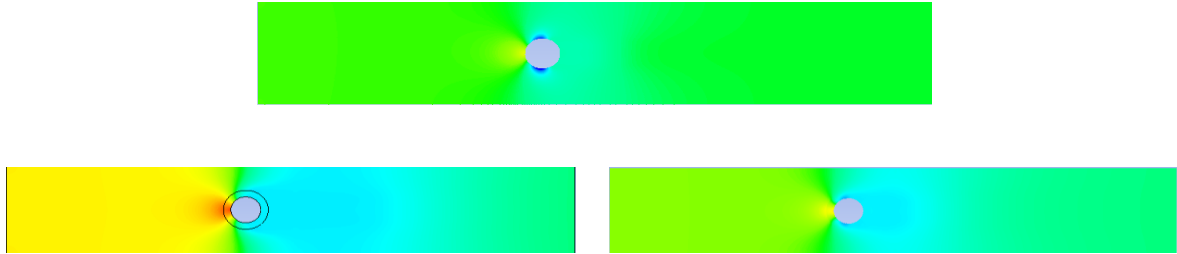
Figure.6. Pressure contours for "bare cylinder, whole and segmented porous layers"at Re = 17000 for 20 PPI and 0.9005
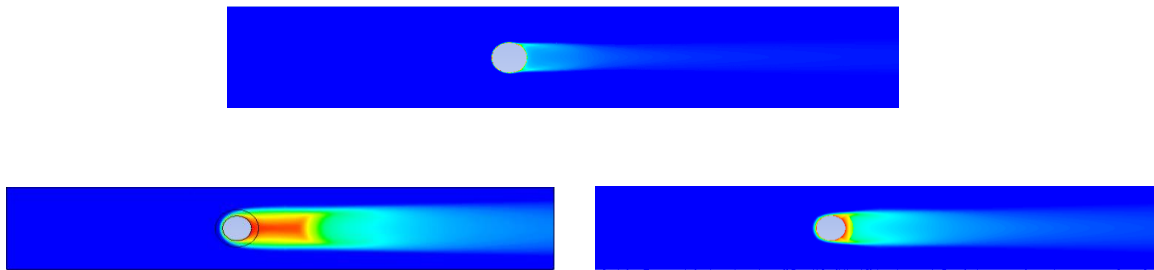
Figure.7. Temperature contours for "bare cylinder, whole and segmented porous layers"at Re = 17000 for 20 PPI and 0.9005 porosity
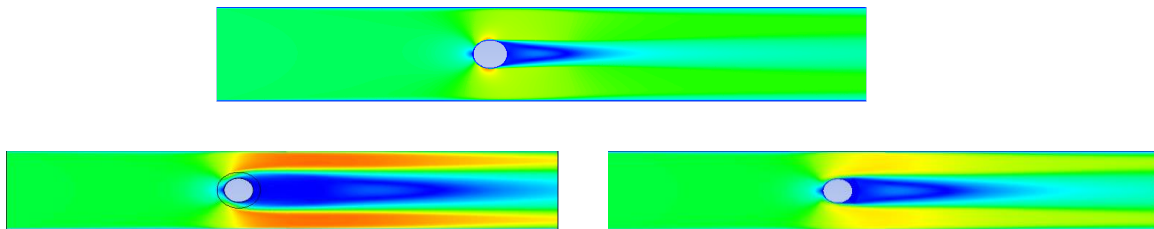
Figure.7. Velocity contours for "bare cylinder, whole and segmented porous layers" at Re = 17000 for 20 PPI and 0.9005

The results of the local velocity contours demonstrate that air reaches the segmented porous zone at a comparatively higher velocity than it does the whole porous layer, where it decelerates dramatically. Due to the exposed region to free stream flow between the front and rear segmented metal foam,

The 20-PPI metal foam is having higher heat transfer augmentation compared to the other case researched due to more surface area for the heat transfer. The Nu no. increases with Re no as predicted but the increases are not linearly and is

mostly because of the metal the metal foam which can also observed from this figure. At less Re no. the buoyancy driven flow dominates while at higher Re no. forced convection dominates predicted. At a particular Re no., the Nu no.rises with PPI of the metal foam. As observed in Figures 9 and figure 11, the average Nu no. increases dramatically when a metal foam case is applied to on bare case, and the entire porous layer outperforms the segmented porous case because to the surplus metal foam around the bare cylinder.

At highest Re no i.e., Re= 19000 the whole porous layer enhances the Nu no. by factor of 5.84 times the bare cylinder case for pore density 20 with porosity 0.9005.

For the same case segmented porous layer enhances the Nu no by factor of 3.47 times the bare cylinder case for pore density 20 with porosity 0.9005.

It can also observe that as Re increases, the augmentation slope lowers, and if stretched, it would most likely achieve an asymptotic, as David et al. concluded (2002).

3.2. Pressure drops effect

The pressure drop effects may be investigated by studying the pressure coefficient (Cp) on the cylinder surface , which

Figure.10. Nu no. vs Re no. for the "segmented porous layer

Figure.8. Nu no. vs Re no. for the "whole porous layer and bare cylinder"
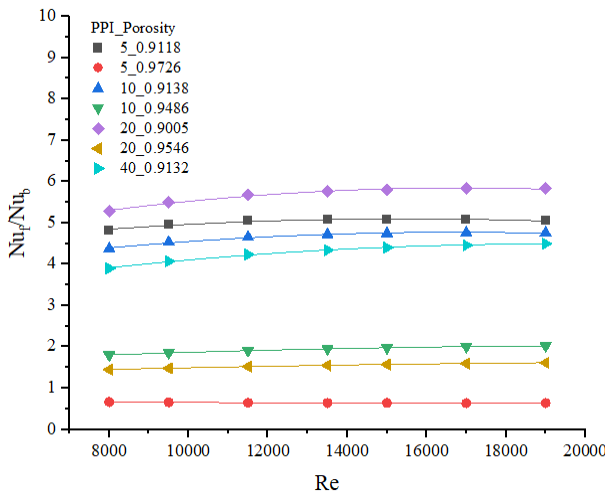
Figure.9. Nusselt number ugmentation ratio ("Nu$_f$/Nu$_b$") for the "Whole Porous layer"
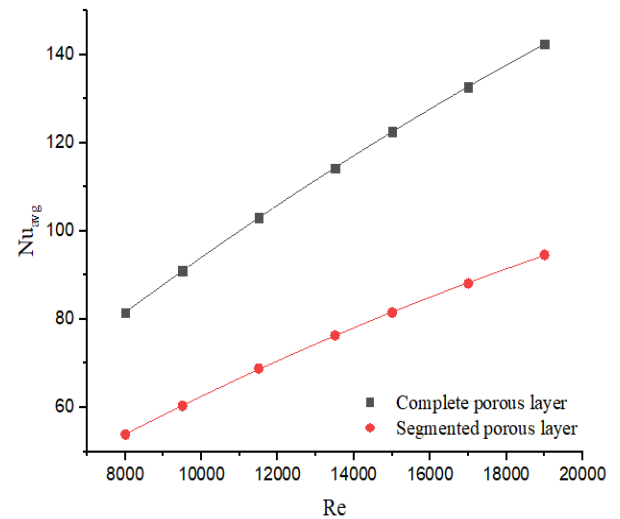
Figure.11. Nu for the "whole porous and segmented porous layer"for pore density 20 with porosity 0.9005

reflects the pressure drop around the cylinder's perimeter, and the net drag coefficient (Cd) produced on the cylinder, which

is a flow resistance calculation. The coefficient expressions are as follows:

$$C_D = \frac{F_N}{\frac{1}{2}\rho V^2_\infty} + \frac{F_T}{\frac{1}{2}\rho V^2_\infty}$$

According to this analysis as the pore density is increases more will be pressure drop. Also, lesser porosity has more effect on pressure drop. For the case 40 PPI with porosity 0.9132 has higher pressure drop and for case 5 PPI with 0.9728 has lower pressure drop.

3.3. Drag coefficient

The form coefficient is one of two main hydraulic characteristics of the porous medium. It is determined by the shape or form of the fibre or solid section of the porous obstacle (Lage et al. 2005). The drag coefficient (CD), as shown in Equation (15), is made up of 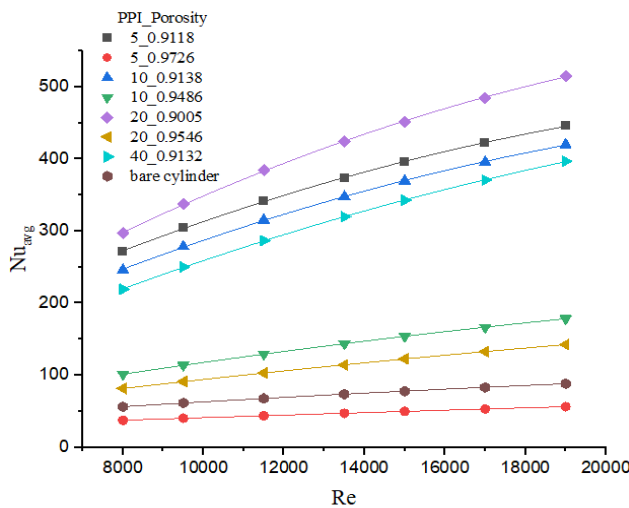two components: the first is an expression of the forces owing to the local pressure components in the flow direction, represented by (Cpx), and the second is an expression of the forces related to shear stress at the cylinder surface.
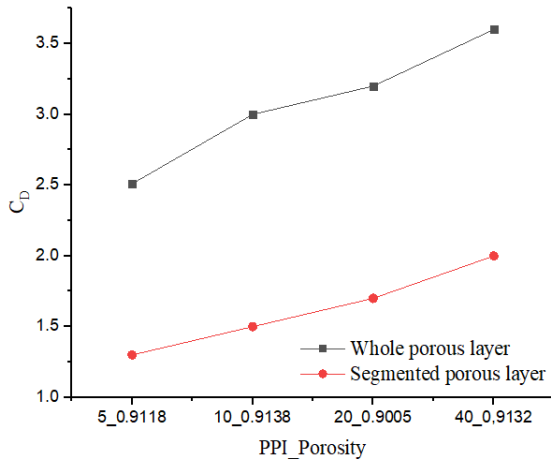
Figure.12. Drag coefficient for "whole porous and segmented porous layer"

All porous layer case clearly showed greater drag force than that of bare case due to creating more obstacle in the direction of fluid flow. However, it is exciting to see that the "coefficient of drag" of the segmented porous case is greater than that of the bare casebut less than whole porous layer case Drag coefficient for whole porous and segmented porous layer shown in fig 12.

Moreover, as a result of the zig-zag path of metal foams, the flow flowing inside the foam is significantly slowed, though in a turbulent mixing manner, reducing the existence of a sharp velocity differential in the boundary layer around the cylinder.

Consequently, when the two components of drag are combined, the entire porous layer would generate substantially stronger drag forces, which would boost the "C_D" to about two times that of a bare case. While the segmented porous case contains two mixed components, the presence of metal foam decreases the velocity field surrounding the cylinder's surface,

hence reducing the "skin friction coefficient" to almost the same level as in the case of the whole porous case.

3.4. Enhancement factor Thermal

The thermal enhance factor (TEF) is used to measure the effectiveness of heat transfer which gives by the ratio of the change of heat transfer rate to change in the friction factor and the formula is given by:
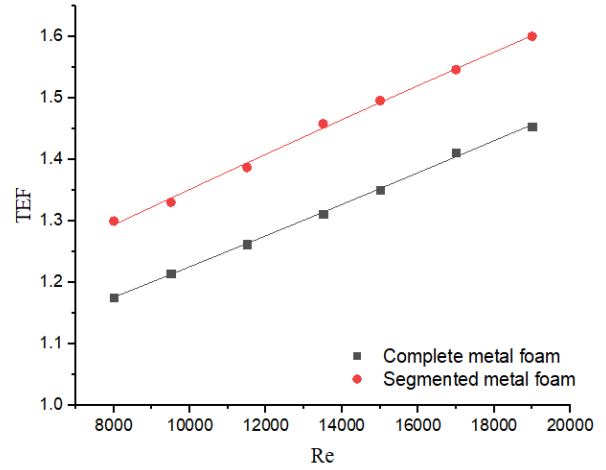
Figure.13. TEF for "whole porous and ase. segmented porous layer"

$$TEF = \frac{\dfrac{Nu_f}{Nu_b}}{\left(\dfrac{f_f}{f_b}\right)^{1/3}}$$

The TEF values for bare cylinder case is 1. As it can clearly seen for all cases segmented metal foam layer gives better heat transfer with less pressure drop as compare to complete metal foam layer c

4. CONCLUSION

In this analytical study of forced convection aroundbare cylinder, complete and segmented porous layer is analysed by using Ansys fluent. The aluminium foam with different-different PPI (5,10.20 and 40 PPI) and porosity range 0.9-0.97 are placed over the cylinder. The main conclusions of this paper are discussed below:

Covering the bare cylinder with complete porous layer gives better result than all cases with the cost of high pressure drop.

The coefficient of heat transfer and Nusselt number rises with pore density as predicted but in this study as shown in figure 13 as porosity increases that means void section increases and effective thermal conductivity also get decreases that means less heat transfer. In this study 20 PPI with 0.9005 porosity gives better result than all other cases. With changes in Reynolds number and Nusselt number different-different regimes can be seen. The segmented porous case, added at the

particularlocation in the study, result to close augmentation values as the whole porous case in terms of heat transfer with less pressure drop, close to the bare case and only between 20% to 50%increase in drag coefficient values for 5 PPI to 40 PPI.

Complete porous layer gives better result but with high pressure drop so to use of segmented metal foam will be more effective in case of heat transfer with less pressure drop and will be more cost effective.

5. RECOMMENDATION

The main focus of this study was to calculate the average Nusselt number over the cylinder in case of bare cylinder, complete porous case and segmented porous case. But the local Nusselt number giver better idea about heat transfer from any surface so this can be done in future for analytically as well as experimentally.

Another recommendation is to do experimentally for segmented porous layer case and compare this result with compact heat exchanger. Also use segmented porous layer in tube bundle would be significant but, in this case, the main focus will be on pumping power requirement.

Also, there is one more possibility to use metal foam as fin this may increase heat transfer with low pressure drop.

REFERENCES

[1] Abu-Al-Saud, B.A., 1997. *Convective heat transfer characteristics in the rectangular packed beds with asymmetric heating* (Doctoral dissertation, King Fahd University of Petroleum and Minerals (Saudi Arabia)).

[2] Ahmed, M.R. and Talama, F., 2008. Flow characteristics and local heat transfer rates for a heated circular cylinder in a crossflow of air. *International Journal of Fluid Mechanics Research*, *35*(1).

[3] Al-Salem, K., Oztop, H.F. and Kiwan, S., 2011. Effects of porosity and thickness of porous sheets on heat transfer enhancement in a cross flow over heated cylinder. *International communications in heat and mass transfer*, *38*(9), pp.1279-1282..

[4] Al-Sumaily, G.F., 2014. Forced convection heat transfer from a bank of circular cylinders embedded in a porous medium. *Journal of heat transfer*, *136*(4).

[5] Al-Sumaily, G.F., Sheridan, J. and Thompson, M.C., 2012. Analysis of forced convection heat transfer from a circular cylinder embedded in a porous medium. *International journal of thermal sciences*, *51*, pp.121-131.

[6] Ashtiani Abdi, I., Hooman, K. and Khashehchi, M., 2014. A comparison between the separated flow structures near the wake of a bare and a foam-covered circular cylinder. *Journal of Fluids Engineering*, *136*(12).

[7] Baliga, B.R. and Patankar, S.V., 1980. A new finite-element formulation for convection-diffusion problems. *Numerical Heat Transfer*, *3*(4), pp.393-409.

[8] Bhattacharya, A., Calmidi, V.V. and Mahajan, R.L., 2002. Thermophysical properties of high porosity metal foams. *International journal of heat and mass transfer*, *45*(5), pp.1017-1031.

[9] Bhattacharyya, S. and Singh, A.K., 2009. Augmentation of heat transfer from a solid cylinder wrapped with a porous layer. *International Journal of Heat and Mass Transfer*, *52*(7-8), pp.1991-2001.

[10] Bhattacharyya, S. and Singh, A.K., 2009. Augmentation of heat transfer from a solid cylinder wrapped with a porous layer. *International Journal of Heat and Mass Transfer*, *52*(7-8), pp.1991-2001.

[11] Boomsma, K. and Poulikakos, D., 2001. On the effective thermal conductivity of a three-dimensionally structured fluid-saturated metal foam. *International Journal of Heat and Mass Transfer*, *44*(4), pp.827-836.

[12] Boules, D., 2020. *Heat Transfer Enhancement from a Horizontal Cylinder Wrapped with a Porous Layer of Metal Foam: Experimental and Numerical Studies* (Doctoral dissertation, University of Guelph).

[13] Boules, D., Sharqawy, M.H. and Ahmed, W.H., 2021. Enhancement of heat transfer from a horizontal cylinder wrapped with whole and segmented layers of metal foam. *International Journal of Heat and Mass Transfer*, *165*, p.120675.

[14] Boyd, B. and Hooman, K., 2012. Air-cooled micro-porous heat exchangers for thermal management of fuel cells. *International Communications in Heat and Mass Transfer*, *39*(3), pp.363-367.

[15] Chen, C.C., Huang, P.C. and Hwang, H.Y., 2013. Enhanced forced convective cooling of heat sources by metal-foam porous layers. *International Journal of Heat and Mass Transfer*, *58*(1-2), pp.356-373.

[16] Chumpia, A. and Hooman, K., 2012, December. Quantification of contact resistance of metal foam heat exchangers for improved, air-cooled condensers in geothermal power application. In *18th Australasian Fluid Mechanics Conference* (pp. 1-4).

[17] De Jaeger, P., T'Joen, C., Huisseune, H., Ameel, B., De Schampheleire, S. and De Paepe, M., 2012. Assessing the influence of four bonding methods on the thermal contact resistance of open-cell aluminum foam. *International journal of heat and mass transfer*, *55*(21-22), pp.6200-6210.

[18] De Paepe, M., Huisseune, H., De Jaeger, P. and T'Joen, C., 2011. The use of open cell metal foams in heat exchangers: possibilities and limitations. *HEFAT 2011*.

[19] Dehghan, M., Valipour, M.S. and Saedodin, S., 2015. Temperature-dependent conductivity in forced convection of heat exchangers filled with porous media: a perturbation solution. *Energy Conversion and Management*, *91*, pp.259-266.

[20] Du, Y.P., Qu, Z.G., Zhao, C.Y. and Tao, W.Q., 2010. Numerical study of conjugated heat transfer in metal foam filled double-pipe. *International journal of heat and mass transfer*, *53*(21-22), pp.4899-4907.

[21] Dukhan, N. and Patel, K., 2011. Effect of sample's length on flow properties of open-cell metal foam

and pressure-drop correlations. *Journal of Porous Materials*, *18*(6), pp.655-665.

[22] Durgam, S., Venkateshan, S.P. and Sundararajan, T., 2017. Experimental and numerical investigations on optimal distribution of heat source array under natural and forced convection in a horizontal channel. *International Journal of Thermal Sciences*, *115*, pp.125-138.

[23] Dyga, R. and Płaczek, M., 2010. Efficiency of heat transfer in heat exchangers with wire mesh packing. *International journal of heat and mass transfer*, *53*(23-24), pp.5499-5508.

[24] Dyga, R. and Płaczek, M., 2015. Heat transfer through metal foam–fluid system. *Experimental thermal and fluid science*, *65*, pp.1-12.

[25] Ettrich, J., August, A. and Nestler, B., 2014. Open cell metal foams: measurement and numerical modelling of fluid flow and heat transfer. *Cellular Materials—CellMat*, pp.1589-84.

[26] Fand, R.M., Varahasamy, M. and Greer, L.S., 1993. Empirical correlation equations for heat transfer by forced convection from cylinders embedded in porous media that account for the wall effect and dispersion. *International journal of heat and mass transfer*, *36*(18), pp.4407-4418.

[27] Fu, H.L., Leong, K.C., Huang, X.Y. and Liu, C.Y., 2001. An experimental study of heat transfer of a porous channel subjected to oscillating flow. *J. Heat Transfer*, *123*(1), pp.162-170.

[28] Fu, W.S. and Huang, H.C., 1997. Thermal performances of different shape porous blocks under an impinging jet. *International Journal of Heat and Mass Transfer*, *40*(10), pp.2261-2272.

[29] Fu, Y., Wen, J. and Zhang, C., 2017. An experimental investigation on heat transfer enhancement of sprayed wire-mesh heat exchangers. *International Journal of Heat and Mass Transfer*, *112*, pp.699-708.

[30] Gallego, N.C. and Klett, J.W., 2003. Carbon foams for thermal management. *Carbon*, *41*(7), pp.1461-1466.

[31] Gangapatnam, P., Kurian, R. and Venkateshan, S.P., 2018. Numerical simulation of heat transfer in metal foams. *Heat and Mass Transfer*, *54*(2), pp.553-562.

[32] Ghorab, M.G., 2015. Forced convection analysis of discrete heated porous convergent channel. *Heat Transfer Engineering*, *36*(9), pp.829-846.

[33] Ghosh, I, 2009. Heat transfer correlation for high-porosity open-cell foam. *International Journal of Heat and Mass Transfer*, *52*(5-6), pp.1488-1494.

[34] Han, X.H., Wang, Q. and Park, Y.G.J., 2012. C., Sommers, A. & Jacobi. *A., A review of metal foam and metal matrix composites for heat exchangers and heat sinks. Heat Transf. Eng*, *33*, pp.991-1009.

[35] Hotta, T.K., Muvvala, P. and Venkateshan, S.P., 2013. Effect of surface radiation heat transfer on the optimal distribution of discrete heat sources under natural convection. *Heat and Mass Transfer*, *49*(2), pp.207-217.

[36] Huang, P.C. and Chen, C.C., 2012. Simulation of mixed convection in a vertical channel containing discrete porous-covering heat blocks. *International journal of heat and mass transfer*, *55*(11-12), pp.3147-3159.

[37] Huisseune, H., De Schampheleire, S., Ameel, B. and De Paepe, M., 2015. Comparison of metal foam heat exchangers to a finned heat exchanger for low Reynolds number applications. *International Journal of Heat and Mass Transfer*, *89*, pp.1-9.

[38] Hunt, M.L. and Tien, C.L., 1988. Effects of thermal dispersion on forced convection in fibrous media. *International Journal of Heat and Mass Transfer*, *31*(2), pp.301-309.

[39] Jeng, T.M. and Tzeng, S.C., 2007. Forced convection of metallic foam heat sink under laminar slot jet confined by parallel wall. *Heat transfer engineering*, *28*(5), pp.484-495.

[40] Kamath, P.M., Balaji, C. and Venkateshan, S.P., 2014. Heat transfer enhancement with discrete heat sources in a metal foam filled vertical channel. *International Communications in Heat and Mass Transfer*, *53*, pp.180-184.

[41] Kasaeian, A., Daneshazarian, R., Mahian, O., Kolsi, L., Chamkha, A.J., Wongwises, S. and Pop, I., 2017. Nanofluid flow and heat transfer in porous media: a review of the latest developments. *International Journal of Heat and Mass Transfer*, *107*, pp.778-791.

[42] Kim, S.Y., Kang, B.H. and Kim, J.H., 2001. Forced convection from aluminum foam materials in an asymmetrically heated channel. *International Journal of Heat and Mass Transfer*, *44*(7), pp.1451-1454.

[43] Kim, S.Y., Paek, J.W., Kang, B.H.: Flow and heat transfer correlations for porous fin in a plate-fin heat exchanger. J. Heat Transf. 122(3), 572–578 (2000)

[44] Kurian, R., Balaji, C. and Venkateshan, S.P., 2016. Experimental investigation of convective heat transfer in a vertical channel with brass wire mesh blocks. *International Journal of Thermal Sciences*, *99*, pp.170-179.

[45] Kurian, R., Balaji, C. and Venkateshan, S.P., 2016. Experimental investigation of near compact wire mesh heat exchangers. *Applied Thermal Engineering*, *108*, pp.1158-1167.

[46] Leong, K.C., Li, H.Y., Jin, L.W. and Chai, J.C., 2011. Convective heat transfer in graphite foam heat sinks with baffle and stagger structures. *Journal of heat transfer*, *133*(6).

Study the Impact of Microfinance Institutions on Poverty Alleviation and Economic Development in India: An Analysis of Loan Repayment Behavior and Social Outcomes.

Anoop Kumar[a] and Shalabh Saxena[b]

[a]Bareilly College Bareilly, Affiliated to M.J.P. Rohilkhand UniversityBareilly (U.P) India – 243006

Email: anoop11dr@gmail.com
[b]Assistant Professor, Department of Business Administration, RIMT Bareilly

*Email: shalabhnov@gmail.com

ABSTRACT

India, with its vast and diverse population, has long grappled with the challenge of bringing its citizens into the formal financial system. MFIs have been instrumental in addressing this issue by providing access to financial services to those previously excluded. They bridge the gap between traditional banks and the unbanked or underbanked, enabling them to save, borrow, and invest. The MFI model, often built on group lending and community-based approaches, has proven effective in reaching remote and marginalized populations.

Poverty remains a pervasive issue in India, affecting millions of households. MFIs offer a lifeline to the poor by extending microloans for income-generating activities, including small businesses, agriculture, and handicrafts. These loans empower borrowers to break the cycle of poverty, improve their livelihoods, and secure a better future for their families. Numerous success stories attest to the transformative impact of microfinance on poverty alleviation in both urban and rural areas.

One of the most remarkable aspects of India's microfinance movement is its focus on women's empowerment. Many MFIs target women as primary clients, recognizing the significant role they play in family and community well-being. By providing women with access to credit, training, and financial education, MFIs empower them to make decisions, become financially independent, and assume leadership roles in their households and communities. This has far-reaching social and economic implications, contributing to gender equality and women's socio-economic upliftment.While the impact of MFIs in India is undeniable, there are challenges that need to be addressed. These include ensuring responsible lending practices, managing interest rates, and preventing over-indebtedness. Regulation and supervision of the microfinance sector are vital to maintain its integrity and protect borrowers.

In conclusion, MFIs in India have proven to be a force for positive change. They have significantly contributed to financial inclusion, poverty reduction, and women's empowerment. However, the sector must continue to evolve and adapt to the changing needs of its clients while adhering to ethical principles.

With the right policies and strategies, India's microfinance institutions can continue to play a transformative role in the socio-economic development of the country, bringing hope and prosperity to millions.

Keywords: microfinance institutions, financial inclusion, poverty alleviation, women's empowerment, group lending, economic upliftment.

1. INTRODUCTION

Microfinance, a financial services innovation that provides small loans, savings, and insurance to economically disadvantaged individuals and communities, has garnered significant attention as a poverty alleviation and economic development tool in India. The practice of microfinance gained prominence in India during the 1970s and has since evolved into a multifaceted industry with a vast network of Microfinance Institutions (MFIs) and Self-Help Groups (SHGs) serving millions of clients.

The significance of microfinance in India is rooted in the country's complex socio-economic fabric. Despite India's remarkable economic growth in recent decades, a substantial portion of its population continues to grapple with poverty, financial exclusion, and limited access to formal financial services. Microfinance emerged as a promising solution to address these challenges by providing access to credit and financial resources for those who are often excluded from traditional banking systems.

The first dimension, poverty alleviation, is a critical concern in India, where a significant portion of the population lives below the poverty line. Microfinance holds the potential to empower the poor by enabling them to start or expand small businesses, meet emergency expenses, and improve their overall quality of life. Assessing the effectiveness of microfinance in alleviating poverty provides invaluable insights into strategies for inclusive growth.

The second dimension, economic development, is equally vital for a country striving to achieve sustainable progress. Microfinance has been recognized as a means to foster economic development by providing capital for income-generating activities, which, in turn, can stimulate local economies and create employment opportunities. Understanding the link between microfinance and economic development is

crucial for policymakers and practitioners seeking to craft effective development strategies.

repayment behavior and social outcomes. Loan repayment behavior is a key indicator of the sustainability of microfinance programs, while the study of social outcomes—such as women's empowerment, improved education, healthcare access, and community development—provides a holistic view of microfinance's broader impact on society.

2. IMPORTANCE

• Poverty remains a pressing issue in India, with a substantial percentage of the population living below the poverty line. Understanding the role of microfinance in poverty alleviation is crucial because it has been recognized as a potential tool to lift people out of poverty. This research can provide insights into the effectiveness of microfinance programs in achieving this goal.

• Economic development is a key indicator of a nation's progress. Microfinance can contribute to economic development by providing access to capital for income-generating activities. Investigating its impact on economic development in India can offer valuable insights into the broader economic landscape.

• Microfinance institutions play a significant role in promoting financial inclusion, especially in regions with limited access to traditional banking services. This research can shed light on how microfinance contributes to expanding financial access and bridging the financial inclusion gap.

• The findings of this research can inform policymakers about the effectiveness of microfinance programs in India. It can help in shaping policies and regulations to support and enhance the impact of microfinance on poverty alleviation and economic development.

• Beyond economic factors, microfinance can have profound social outcomes, such as empowering women, improving education, enhancing healthcare access, and strengthening community development. Understanding these social outcomes is essential for a comprehensive assessment of microfinance's impact.

• Empirical evidence on the impact of microfinance is crucial. By analyzing loan repayment behavior and social outcomes, this research can provide concrete data and insights into the dynamics of microfinance in India, contributing to the empirical literature in the field.

• Investors and donors interested in supporting microfinance initiatives in India rely on research to make informed decisions. Research findings can guide investment strategies and philanthropic efforts aimed at poverty reduction and economic development.

• Assessing the factors that influence loan repayment behavior and the long-term sustainability of microfinance programs is vital. Sustainability ensures that these programs can continue to benefit underserved populations over time.

• The lessons learned from this research in India can have implications beyond its borders. Microfinance is a global phenomenon, and insights from India can inform microfinance programs in other developing countries facing similar challenges.

Microfinance institutions on poverty alleviation and economic development in India is not only academically significant but also holds practical importance for policymakers, practitioners, investors, and the millions of individuals and families seeking to escape poverty and improve their lives. It has the potential to contribute to more effective poverty reduction strategies and sustainable economic development in India and beyond.

3. RESEARCH OBJECTIVES

• To determine the extent to which microfinance institutions (MFIs) in India have contributed to poverty alleviation among their clients.

• To analyze the impact of MFIs on the economic development of their clients, including income growth and asset accumulation.

• To understand the factors that influence loan repayment behavior among microfinance borrowers and assess its implications for the sustainability of microfinance programs.

• To examine the social outcomes associated with microfinance interventions, including women's empowerment, improved education, healthcare access, and community development.

4. RESEARCH QUESTIONS

• To what extent has microfinance contributed to poverty alleviation among its clients in India?

• What is the impact of microfinance on the economic development of its clients in India?

• What factors influence loan repayment behavior among microfinance borrowers in India, and what are the implications for program sustainability?

• What are the social outcomes associated with microfinance in India, and how do they contribute to broader community development?

5. LITERATURE REVIEWS

Microfinance has played a critical role in poverty alleviation and financial inclusion in India. Despite its significance, the microfinance sector faces various challenges in India. These challenges arise from emerging trends in both the microfinance and technology sectors, as well as regulatory changes and supply-side issues [1]. One of the challenges faced by the microfinance sector in India is the problem of multiple borrowing[2].Multiple borrowing refers to the practice of borrowers taking loans from multiple microfinance institutions simultaneously, often leading to over-indebtedness and loan defaults.

This challenge was identified by the "State of the Microcredit Summit Campaign" and is a significant issue in India. To address this challenge, there is a need for better coordination and information sharing among microfinance institutions to identify borrowers who have taken multiple loans.

Unemployment and poverty have posed significant challenges. These issues are primarily rooted in the lack of accessible credit facilities for the underprivileged and jobless individuals.[3] This disparity hampers the nation's pursuit of sustainable development. As India's economy expands, the wealth gap widens. Microfinance emerges as a crucial solution, offering loans that empower the poor to create businesses and assets, ultimately breaking free from poverty.

Over the past two decades, India has made substantial strides in delivering sustainable financial services to the impoverished. These loans aim to foster long-term financial independence and sustainable development, playing a pivotal role in achieving economic growth and poverty reduction. This paper delves into the challenges and recommended strategies for fostering the growth of microfinance in India to facilitate sustainable development.

Microfinance based on the financial needs of the poor, addresses constraints, and discusses formal-informal financial system linkages and various microfinance models in India. It highlights that while the formal system offers large, cheap funding, informality provides flexible transactions.[4] The paper compares individualistic and cooperative approaches, SHGs, BGGs, Federations, and Cooperatives. It suggests SHGs promote empowerment and self-reliance, while cooperatives may favor wealthier individuals. In India, microcredit faces challenges, with many banks having low Credit-Deposit ratios. Informal markets resurged in rural areas in 1991 after a decline in 1981.

6. RESEARCH METHODOLOGY

As this is a descriptive study, secondary data is used as the foundation for this paper. Data is gathered from books, various websites, periodicals, newspapers, NABARD-published RRB reports, Asian Development Bank publications, and fresh research articles published on various websites.

7. PROBLEM & CHALLENGES OF MICROFINANCE IN INDIA

The Reserve Bank of India (RBI) is the central bank of India and plays a crucial role in regulating and supervising the financial sector, including fintech companies.[8] While fintech has the potential to bring financial inclusion and innovation, there are challenges and concerns that need to be addressed, especially in rural areas where people may be more vulnerable. However, attributing suicide among rural individuals solely to the influence of foreign financing companies is a complex issue. Here are some key aspects to consider:

- Fintech companies, including foreign-based ones, often operate in a regulatory gray area, which can lead to predatory lending practices, high-interest rates, and inadequate consumer protection. The RBI has a responsibility to regulate and supervise these entities, but it can be challenging to keep pace with the fast-evolving fintech industry.
- Some foreign financing companies may use aggressive marketing and lending strategies to target vulnerable populations in India, including rural areas. This can lead to individuals taking on unsustainable levels of debt, which can contribute to financial stress.
- Over-indebtedness, driven by multiple loans or high-interest rates from various fintech lenders, can create a severe financial burden on individuals in rural areas. This financial stress can lead to depression and other mental health issues, which can contribute to suicides.
- Rural individuals may have limited financial literacy and may not fully understand the terms and conditions of the loans

they are taking. This lack of understanding can lead to poor financial decision-making and contribute to their vulnerability.
- Rural individuals often rely on agriculture, which is susceptible to factors like crop failures and price fluctuations. When these economic challenges occur, the pressure to repay loans can increase, potentially leading to financial distress.
- The absence of effective grievance redressal mechanisms for borrowers facing issues with fintech companies can contribute to a sense of helplessness and frustration.

To address these issues, it's important for the RBI to strengthen its regulatory oversight of fintech companies, especially those engaging with rural populations. This could include setting caps on interest rates, ensuring transparent lending practices, and promoting financial literacy initiatives. Additionally, the government and civil society organizations should work on programs to improve the financial literacy of rural individuals and provide support for those facing financial distress.

While foreign financing companies can play a role in these challenges, it's essential to recognize that the issue is multifaceted and not solely the result of foreign influence. The root causes are often deeply intertwined with economic, social, and regulatory factors that need to be addressed comprehensively to prevent financial distress and its tragic consequences.

8. MICRO-FINANCE IN INDIA

Microfinance refers to a financial service tailored for individuals or groups with limited income, offering access to financial resources that would otherwise be unavailable to them. This approach enables people to secure small business loans while adhering to ethical lending standards. In India, two primary methods exist for providing microfinance services: the Bank-led approach, known as Self Help Group–Bank Linkage Programme (SHG-BLP), and the Micro Finance Institution (MFI) led approach.

India's microfinance sector is diverse, encompassing various entities delivering financial services, including credit, insurance, and pension options to low-income households. These entities fall into five main categories: Banks, NBFC-MFIs, Small Finance Banks, NBFCs, and Non-profit MFIs. With the exception of Non-profit MFIs, these entities are regulated by the Reserve Bank of India (RBI). Non-profit MFIs typically operate under Societies or Trusts and are regulated by relevant Acts. Additionally, voluntary organizations and NGOs have played a crucial role as financial intermediaries, often assisting Self Help Groups (SHGs) in forming federations. These federations fulfill essential non-financial roles such as social and capacity building, SHG promotion training, internal audit, and establishing links for backward and forward integration.
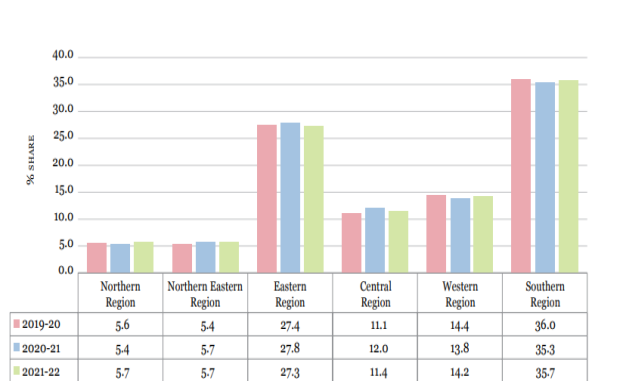
The Eastern region showed the most significant growth with a 75% increase in savings, followed by the Central region with a 53% rise. Conversely, the Western region saw a decline of 12%. Regarding the percentage distribution of SHGs savings linked in the mentioned year, the Southern region led with a 36% share, trailed by the Eastern region at 27.4% and the Western region at 11.4%.

Table.2.2. Region-wise progress of Savings Linked SHG's with Banks (2020-21 to 2022-23)

(₹ lakh)

Sr. No.	Regions	2019-2020		2020-21		2021-22	
		No. of SHGs	Savings-Amount	No. of SHGs	Savings-Amount	No. of SHGs	Savings-Amount
A	Northern	5,77,122	59,550	6,09,808	1,74,345	6,80,143	1,99,582
B	North Eastern	5,56,899	48,141	6,33,714	83,126	6,80,845	1,06,441
C	Eastern	28,11,130	6,64,333	31,22,424	7,74,912	32,43,980	13,58,595
D	Central	11,35,083	1,71,217	13,45,575	2,11,870	13,55,564	3,25,696
E	Western	14,73,853	2,01,880	15,50,176	3,74,023	16,88,451	3,27,691
F	Southern	36,89,236	14,70,085	39,61,703	21,29,485	42,44,070	24,06,043
	Total	1,02,43,323	26,15,206	1,12,23,400	37,47,761	1,18,93,053	47,24,048

Source : Status of Microfinance in India, 2019-20 to 2021-22

Detailed state-wise information about the number of SHGs linked with banks can be found in Statement IIA.

	Northern Region	Northern Eastern Region	Eastern Region	Central Region	Western Region	Southern Region
2019-20	5.6	5.4	27.4	11.1	14.4	36.0
2020-21	5.4	5.7	27.8	12.0	13.8	35.3
2021-22	5.7	5.7	27.3	11.4	14.2	35.7

Source: STATUS OF MICROFINANCE IN INDIA 2021-22

Figure.2.3. Region-wise share in number of savings linked SHG's

Following the upward trend in savings linkage observed throughout the year, the cumulative savings of Self-Help Groups (SHGs) with banks increased by 26%, rising from Rs. 374.78 lakh crore in 2020-21 to Rs. 472.40 lakh crore in 2021-22.

Evaluating the financial health and discipline of SHGs, the outstanding savings position is a crucial indicator. Geographically, every region experienced positive growth. On a state level, 16 States/UTs showed growth rates surpassing the national average, while 7 (Arunachal Pradesh, Chhattisgarh, Lakshwadweep, Maharashtra, Meghalaya, New Delhi, and Punjab) lagged behind.

The average savings per SHG rose by 31%, from Rs. 33392 in 2020-21 to Rs. 39721 in 2021-22. Region-wise data indicates increased average savings in all regions except the Western region, where it decreased. Notably, the Eastern region saw a significant 69% rise (from Rs. 24,818 to Rs. 41,881). The Southern and North-Eastern regions maintained the highest and lowest average savings per SHG, respectively. Among States/UTs, Punjab led with an outstanding average savings of Rs. 1.53 lakh per SHG. Detailed state-wise savings data can be found in Statement IIA.

9. CREDIT DISBURSEMENT BY BANKS

Banks provided loans totaling Rs. 99729 crore to 34 lakh Self Help Groups (SHGs) in the fiscal year 2021-22, as opposed to Rs. 58071 crore extended to 29 lakh SHGs in 2020-21. This represents a significant increase of 72% in the amount of credit disbursed and an 18% growth in the number of SHGs linked to credit during the year. You can find a detailed comparison of bank loans disbursed to SHGs over the past three financial years (2019-20 to 2021-22) in Table 2.3. [6]

Table.2.3. Region-wise status of Bank Loan Disbursed to SHG's during 2022-23

(₹ lakh)

Region	2019-2020			2020-21			2021-22		
	No. of SHGs	Total Loans Disbursed	Average Loan Disbursed	No. of SHGs	Total Loans Disbursed	Average Loan Disbursed	No. of SHGs	Total Loans Disbursed	Average Loan Disbursed
Northern	62,905	84,694	1,34,637	67,658	94,045	1,39,001	79,532	1,17,102	1,47,239
North Eastern	37,807	57,893	1,53,128	68,116	1,03,651	1,52,168	94,871	1,84,636	1,94,618
Eastern	11,23,517	17,85,075	1,58,883	11,24,578	14,87,551	1,32,276	13,01,505	25,68,978	1,97,385
Central	1,11,074	1,04,249	93,856	1,28,617	1,05,428	81,971	1,84,322	2,16,983	1,17,720
Western	1,74,218	2,49,327	1,43,112	1,61,159	2,30,331	1,42,921	2,39,086	3,81,363	1,59,509
Southern	16,36,481	54,84,696	3,35,152	13,37,266	37,86,063	2,83,120	14,98,951	65,03,860	4,33,894
Total	31,46,002	77,65,935	2,46,851	28,87,394	58,07,068	2,01,118	33,98,267	99,72,923	2,93,471

Source: Status of microfinance in india 2021-22

Credit disbursement to Self Help Groups (SHGs) during the fiscal year 2021-22 exhibited growth in all regions compared to 2020-21, with the Central region experiencing the most substantial increase of 106%.

The Southern region recorded the highest disbursement, extending Rs. 65039 crore to 15 lakh SHGs, while the Northern region had the lowest disbursement, providing Rs. 1171 crore to 0.8 lakh SHGs.

A comparative analysis of the region-wise percentage share in SHG credit linkage over the past three years (2019-2020 to 2021-22) reveals that the North Eastern Region (NER), Central Region, and Western Region have increased their share. However, there is an observed decline of nearly 8 percentage points in the share of the Southern region from 2019-2020 to 2021-22.[5]

In contrast, the share of the Northern and Eastern regions has remained relatively constant (Fig. 2.5). In the current year, the Southern region boasts the highest percentage of SHGs with linked credit at 44.11%, closely followed by the Eastern region at 38.30%. The proportion of SHGs with linked credit in the Northern, North Eastern, Central, and Western regions remains below 8%.

10. CREDIT OUTSTANDING

As of March 31, 2022, a grand total of 67 lakh Self Help Groups (SHGs) with linked credit had outstanding loans amounting to R1,51,051.30 crore (see Table 2.4).[6] On average, each SHG had an outstanding loan of approximately R2.24 lakh at the national level.

Table .2.4 Region-wise SHG's having Loans Outstanding (As on 31 March 2022)

			(₹ lakh)	
Sr. No.	Regions	SHGs credit linked (No.)	Loans outstanding with SHGs	
			Total	Per SHG
1	Northern Region	1,61,848	1,65,378	1.02
2	North Eastern Region	2,12,009	2,36,245	1.11
3	Eastern Region	24,59,218	35,29,425	1.44
4	Central Region	4,07,004	3,25,178	0.80
5	Western Region	3,91,082	4,49,277	1.15
6	Southern Region	31,08,796	1,03,99,627	3.35
7	**Total**	**67,39,957**	**1,51,05,130**	**2.24**

Source: Status of Microfinance in India 2021-22

In terms of regional distribution, the Southern region held the highest cumulative outstanding loan balance as of March 31, 2022, both in total and on a per-SHG basis. The credit linkage status of Self Help Groups (SHGs) in each state as of March 31, 2022, is illustrated in Figure 2.7.[6]

Out of the total 118.93 lakh SHGs with linked savings, 57% of these groups have outstanding loans with banks. Nine states have a credit linkage percentage higher than the national average. Andhra Pradesh leads with 90% of its SHGs having outstanding loans, followed closely by Bihar (89%) and Karnataka (87%). The Southern and Eastern states, alongside Tripura, are prominently featured in this list.
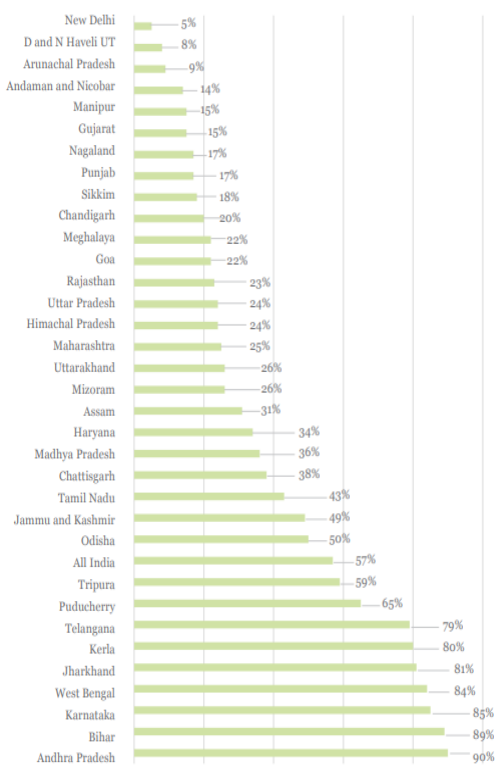
Figure.2.7. State-wise SHG's with credit linkage (As on 31.03.22)

Furthermore, the average outstanding loan size as of March 31, 2022, has increased in all states compared to the previous year's data. The most significant increase was observed in Chandigarh (432%), followed by Jharkhand (155%) and Manipur (139%).

11. AGENCY WISE DISTRIBUTION OF SHG BANK LINKAGE PROGRAMME

Commercial Banks, Regional Rural Banks (RRBs), and Cooperative Banks play a crucial role in bolstering the Self Help Group-Bank Linkage Programme (SHG-BLP) by offering savings and credit services. The status of the SHG-BLP, broken down by agency, can be found in Table 2.5.[6] As of March 31, 2022, Commercial Banks have performed exceptionally, with more than 69 lakh SHGs holding savings accounts with them through their extensive banking network.

Table.2.5. Agency-wise status of SHG-BLP in 2021-22

								(₹ lakh)
Category of Agency	Total Savings of SHGs with Banks as on 31 March 2022		Loans disbursed to SHGs by Banks during 2021-22		Total Outstanding Bank Loans against SHGs as on 31.03.2022		NPAs as on 31.03.2022	
	No. of SHGs	Savings Amount	No. of SHGs	Loans disbursed	No. of SHGs	Loan Outstanding	Amount of Gross NPA	NPA (%)
Commercial Banks	68,87,508	30,72,648	20,79,254	61,22,577	41,81,656	1,02,65,757	3,31,856	3.23
% Share	57.91	65.04	61.19	61.39	62.04	67.96	57.78	
RRBs	35,83,219	13,79,125	11,05,178	32,59,124	20,29,015	39,48,866	1,24,172	3.14
% Share	30.13	29.19	32.52	32.68	30.10	26.14	21.62	
Cooperative Banks	14,22,326	2,72,275	2,13,835	5,91,221	5,29,286	8,90,507	1,18,343	13.29
% Share	11.96	5.76	6.29	5.93	7.85	5.90	20.60	
Total	1,18,93,053	47,24,048	33,98,267	99,72,923	67,39,957	1,51,05,130	5,74,371	3.80

Source: Status of microfinance in india 2021-22

Therefore, concerning the number of Self Help Groups (SHGs) maintaining savings accounts with banks, Commercial Banks are at the forefront with a majority share of 58%, followed by Regional Rural Banks (RRBs) at 30% (35.83 lakh SHGs) and Cooperative Banks at 12% (14.22 lakh SHGs).[7] Detailed information about savings outstanding as of March 31, 2022, for each bank is provided in Statement IA.

Commercial Banks also dominate in terms of disbursed loans and outstanding loans related to SHGs. Specific data regarding loans provided to SHGs and the corresponding outstanding amounts can be found in Statements I-B and I-C, respectively.

Table.2.6. Agency-wise Average Savings, Loan Disbursement per SHG

									₹ Lakh)
Category of Agency	Average Savings of SHGs with Banks			Average Loans disbursed to SHGs by Banks			Average Outstanding Bank Loans against SHGs		
	2021-22	2020-22	Change (%)	2021-22	2020-22	Change (%)	2021-22	2020-22	Change (%)
Commercial Banks	44,612	36,872	20.99	2,94,460	1,91,806	53.52	2,45,495	1,85,768	32.15
Regional Rural Banks	38,488	26,445	45.54	2,94,896	2,06,742	42.64	1,94,620	1,76,724	10.13
Cooperative Banks	19,143	35,838	-46.58	2,76,485	2,29,278	20.59	1,68,247	1,43,248	17.45
Total	39,721	33,392	18.95	2,93,471	2,01,118	45.92	2,24,113	1,78,694	25.42

Source: Status of microfinance in india 2021-22

As indicated in Table 2.6, the typical savings held by Self Help Groups (SHGs) in various agencies have risen, except for Cooperative Banks, which experienced a significant 47% decrease. The average savings have increased from Rs. 33,392 in 2020-21 to Rs. 39,721 in 2021-22. Furthermore, the average loans extended to SHGs have surged by 45.92% compared to the previous year, with an increase observed across all agencies.

12. FAILURES OF RBI IN CONTROLLING FINTECH IN MICROFINANCE IN INDIA FOR RURAL SOCIETY:

• The RBI has struggled to keep pace with the rapid growth of fintech in microfinance. The absence of a comprehensive regulatory framework tailored to these emerging technologies has allowed predatory lending practices, excessive interest rates, and a lack of consumer protection, particularly in rural areas.

• Weak enforcement of existing regulations and limited oversight of fintech companies operating in microfinance have created a situation where compliance issues, unscrupulous practices, and over-indebtedness often go unchecked, disproportionately affecting vulnerable rural borrowers.

• The RBI has not been as proactive as needed in promoting financial literacy programs in rural areas. This gap in education exacerbates the vulnerability of borrowers who may not fully comprehend the terms and consequences of the loans they take.

13. CONCLUSION

In conclusion, the two dimensions of microfinance, namely poverty alleviation and economic development, hold significant importance in the context of India's socio-economic landscape. Microfinance has the potential to be a powerful tool for empowering the impoverished population, helping them establish small businesses, manage unforeseen financial challenges, and enhance their overall quality of life. Evaluating the impact of microfinance on poverty alleviation provides valuable insights for promoting inclusive growth in the country.

Similarly, microfinance also plays a vital role in fostering economic development. By providing access to capital for income-generating activities, it can stimulate local economies and generate employment opportunities, contributing to the overall economic progress of the nation. Understanding the intricate relationship between microfinance and economic development is crucial for policymakers and practitioners as they work towards crafting effective and sustainable development strategies for India.

Microfinance has emerged as a powerful tool in addressing both poverty alleviation and economic development in India. By providing financial services to the poor, microfinance enables them to break free from the cycle of poverty and improve their standard of living. Microfinance plays a significant role in stimulating local economies and creating employment opportunities, contributing to sustainable economic development. The effectiveness of microfinance in these dimensions provides valuable insights for policymakers and practitioners, emphasizing the need for inclusive growth strategies.

14. SUGGESTIONS

Suggestions for RBI to Control Fintech in Microfinance and Prevent Rural Suicides:

• The RBI should establish and enforce stringent regulations specific to fintech in microfinance, setting clear guidelines on interest rates, fair lending practices, and risk assessment. This will ensure that rural borrowers are protected from predatory lending practices.

• Invest in comprehensive financial literacy initiatives, particularly in rural communities, to empower borrowers with the knowledge and skills necessary to make informed financial decisions and manage their debt effectively.

• The RBI should create efficient grievance redressal mechanisms, ensuring that rural borrowers have avenues to voice their concerns and seek resolution when they face difficulties with fintech microfinance providers.

• Foster collaboration between the RBI, fintech companies, and local stakeholders to work together in addressing the unique challenges faced by rural borrowers. This could lead to more responsible lending practices and better support for those in financial distress, ultimately reducing the risk of rural suicides.

REFERENCES:-

[1] Sinha, G. (2015, July 1). Responding to Complexity: Microfinance MIS Service Providers as Complex Adaptive Systems .https://scite.ai/reports/10.1177/2393957515597583

[2] Gupta, P K., & Sharma, S. (2021, July 8). Literature review on effect of microfinance institutions on poverty in South Asian countries and their sustainability. https://scite.ai/reports/10.1108/ijoem-07-2020-0861

[3] K. Sanjeeb and Dey, "Challenges & Issues of Microfinance in India," *Online)*, vol. 6, no. 7, 2015, Available: https://core.ac.uk/download/pdf/234646976.pdf

[4] R. Dasgupta and K. D. Rao, "Microfinance in India: Issues, Challenges and Policy Options," *Savings and Development*, vol. 27, no. 2, pp. 203–237, 2003, Accessed: May 27, 2023. [Online]. Available: https://www.jstor.org/stable/25830826

[5] H. Knewtson and H. Qi, "Managing risk for sustainable microfinance", *J. Risk Finance*, vol. 20, no. 1, pp. 2–13, Jan. 2019. Accessed: Oct. 16, 2023. [Online]. Available: https://doi.org/10.1108/jrf-05-2018-0075

[6] Status of Microfinance in India 2021-22 | NABARD."Nabard.org.https://www.nabard.org/auth/writeaddata/tender/2707225843somfi-2021-22-final-english.pdf.

[7] M. Rathore, "India: Savings linked share under SHG-BLP by Bank Type 2022," Statista, https://www.statista.com/statistics/1326067/indiasavings-linked-share-shg-blp-by-bank-type/ (accessed Oct. 12, 2023).

[8] MasterDirections."rbi.org.in. rbi.org.in/Scripts/BS_ViewMasDirections.aspx?id=12256 (accessed July 25 2022).